

Journal Pre-proof

Sonophotocatalytic activities of FeCuMg and CrCuMg LDHs: Influencing factors, antibacterial effects, and intermediate determination

Tannaz Sadeghi Rad, Zahra Ansarian, Reza Darvishi Cheshmeh Soltani, Alireza Khataee, Yasin Orooji, Fatemeh Vafaei



PII: S0304-3894(20)31051-7

DOI: <https://doi.org/10.1016/j.jhazmat.2020.123062>

Reference: HAZMAT 123062

To appear in: *Journal of Hazardous Materials*

Received Date: 25 February 2020

Revised Date: 23 May 2020

Accepted Date: 25 May 2020

Please cite this article as: { doi: <https://doi.org/>

This is a PDF file of an article that has undergone enhancements after acceptance, such as the addition of a cover page and metadata, and formatting for readability, but it is not yet the definitive version of record. This version will undergo additional copyediting, typesetting and review before it is published in its final form, but we are providing this version to give early visibility of the article. Please note that, during the production process, errors may be discovered which could affect the content, and all legal disclaimers that apply to the journal pertain.

© 2020 Published by Elsevier.

Sonophotocatalytic activities of FeCuMg and CrCuMg LDHs: Influencing factors, antibacterial effects, and intermediate determination

Tannaz Sadeghi Rad,^b Zahra Ansarian,^b Reza Darvishi Cheshmeh Soltani,^c Alireza Khataee,^{b,d,e,*} Yasin Orooji,^{a,*} Fatemeh Vafaei^f

^aCollege of Materials Science and Engineering, Nanjing Forestry University, Nanjing 210037, China

^bResearch Laboratory of Advanced Water and Wastewater Treatment Processes, Department of Applied Chemistry, Faculty of Chemistry, University of Tabriz, 51666-16471 Tabriz, Iran

^cDepartment of Environmental Health Engineering, School of Health, Arak University of Medical Sciences, 38196-93345 Arak, Iran

^dDepartment of Environmental Engineering, Gebze Technical University, 41400 Gebze, Turkey

^eInstitute of Research and Development, Duy Tan University, Da Nang 550000, Vietnam

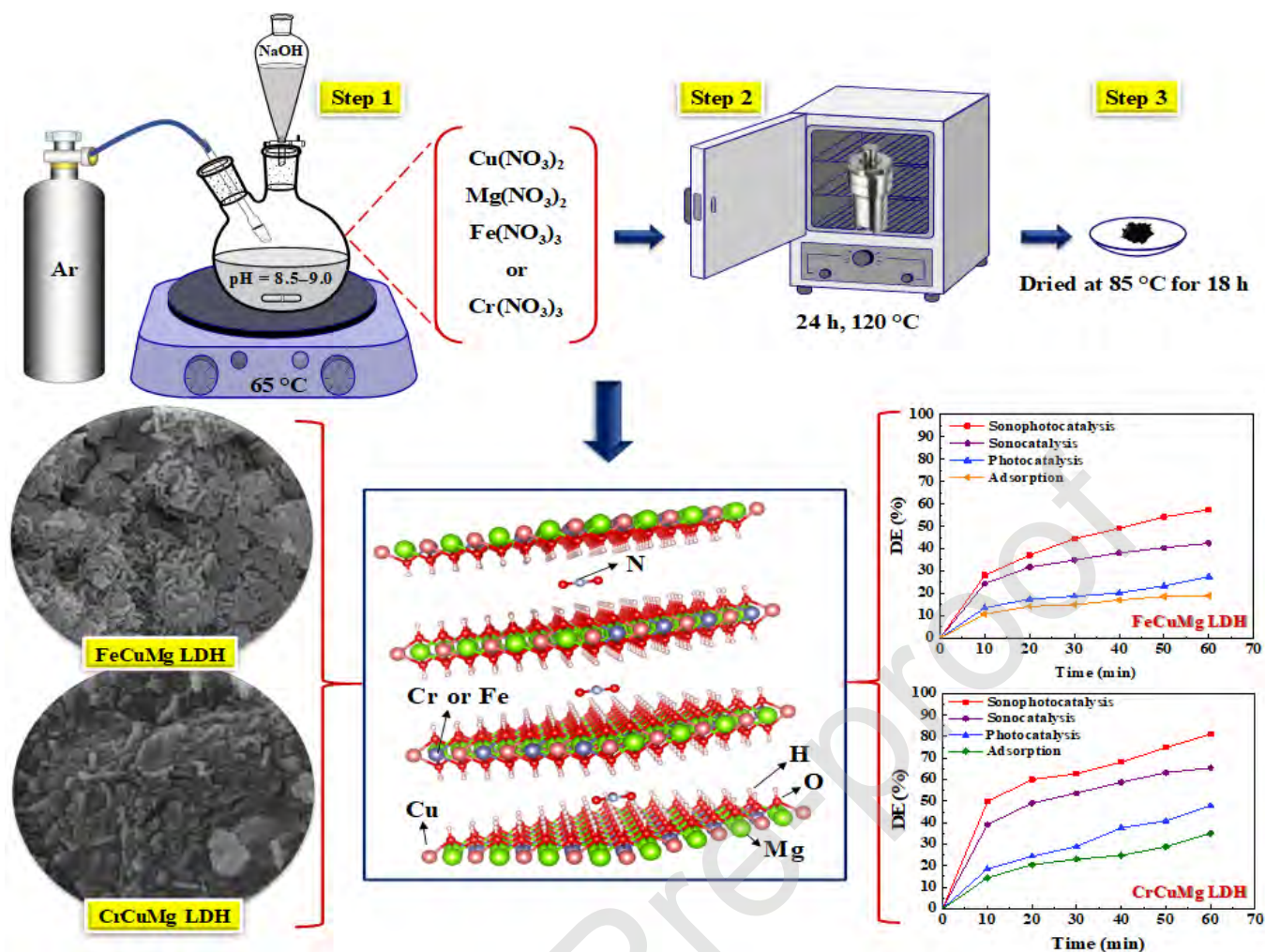
^fCentral Laboratory of the University of Tabriz, University of Tabriz, 51666-16471 Tabriz, Iran

* Corresponding authors:

Email: a_khataee@tabrizu.ac.ir, alirezakhataee@duytan.edu.vn (A. Khataee)

yasin@njfu.edu.cn (Y. Orooji)

Graphical abstract



Highlights

- Fabrication of CrCuMg and FeCuMg LDHs through a simple hydrothermal method.
- Studying the activity of as-prepared catalysts for the sonophotocatalysis of AB113.
- Evaluation of variables as well as LDH analyses and byproduct identifications.
- The antibacterial assessment of as-synthesized LDHs through MIC and CFU methods.

Abstract

Herein, FeCuMg and CrCuMg layered double hydroxides (LDHs) were synthesized and their sonophotocatalytic activities toward Acid blue 113 (AB113) were compared. Sonolysis alone (only ultrasound) led to the decolorization efficiency of 13.0%. A similar result was obtained in the case of the utilization of photolysis alone using a 10-W LED lamp (13.5%). The adsorption process of AB113 onto both compounds was not efficient to significantly remove the target contaminant. The bandgap energy of 2.54 eV and 2.41 eV was calculated for FeCuMg and CrCuMg LDHs, respectively, indicating relatively higher photocatalytic activity of Cr-incorporated LDH than FeCuMg LDH. The sonophotocatalysis of AB113 (50 mg L⁻¹) over CrCuMg LDH (81.1%) was more efficient than that of FeCuMg LDH (57.3%) within the reaction time of 60 min. Intermediate byproducts of the sonophotocatalytic decomposition of organic dye over the as-synthesized tri-metal layered sonophotocatalysts were also identified. Furthermore, the antibacterial activity of both LDHs was evaluated by the CFU technique and the MBC and MIC values were determined. The antibacterial assessment confirmed the higher antibacterial activity of CrCuMg LDH than that of FeCuMg LDH against *Staphylococcus aureus* (*S. aureus*).

Keywords: Sonophotocatalysis; Advanced oxidation process; Tri-metal layered double hydroxide; Dye degradation.

1. Introduction

The utilization of inorganic layered materials with well-ordered structures provides special properties for solving clean-energy problems and recent environmental issues [1]. Layered double hydroxide (LDH) is an important class of layered materials, known as a naturally arising hydrotalcite-like compound used for the exchange of various anionic compounds, photocatalysis, polymerization, photochemistry, medical applications, adsorption of organic

and inorganic pollutants as well as catalytic conversion of various contaminants [2, 3]. This compound is widely applied as an effective catalyst and the precursor of catalyst for the catalytic treatment systems [4-6]. Typically, LDH is a two-dimensional nanostructure composed of positively charged metal hydroxides which are charge-balanced [7]. The brucite-like layers of LDH contain abundant basic sites allowing the compound to be applied as a solid base heterogeneous catalyst with high specific surface area, suitable chemical stability, and remarkable flexibility [8, 9]. In addition, two or three metals placed in the brucite-like layers are uniformly distributed at the atomic level in which one of the metal cations is a catalytically active transition metal with high catalytic properties [10, 11]. In the structure of LDH, divalent cations are replaced with trivalent cations, which results in the formation of a positively charged layered structure [12]. The positive charge of the structure is balanced by the anions incorporated into the interlayer [13].

Clean water is a necessity for a healthy society to attain sustainable development. Increasing agricultural and industrial activities lead to increased demand for new water resources and the decontamination of existing resources [14]. However, the contamination of water resources by industrial effluents containing heavy metals and organic dyes is causing serious environmental concerns [3]. Moreover, the presence of organic dyes in water resources brings about toxicity in aquatic life and subsequently, human consumers due to their carcinogenic nature [15, 16].

Advanced oxidation processes (AOPs) based on the production of hydroxyl radical ($\cdot\text{OH}$) have received great attention in recent years because of their high efficiency to decompose persistent organic compounds [17, 18]. Amongst, sonocatalytic treatment processes based on the application of ultrasound in the presence of an appropriate sonocatalyst generating $\cdot\text{OH}$ has gained great attention for the degradation of emerging pollutants [19]. In this case, the LDHs are considered as potential sonocatalysts. Heterogeneous photocatalysis is also one of the most

promising treatment techniques in environmental remediation [20]. Regarding photocatalysis, the catalytic performance of the LDHs is verified [21].

The combined AOP techniques such as the combination of the sonocatalysis with the photocatalysis named “sonophotocatalysis” have recently been received attention to treat refractory wastewater pollutants [21, 22]. Additionally, the sonophotocatalytic process is able to degrade a wide range of organic contaminants efficaciously. Synergistically, the degradation efficiency is boosted with the merging of ultrasonic waves with light irradiation in the extraordinarily reactive media [12]. Furthermore, the overall mineralization mechanism includes the formation of reactive oxygen species (ROSs) including $\cdot\text{OH}$ and superoxide ($\text{O}_2^{\cdot-}$) radicals which can decompose the contaminants into less hazardous acids, alcohol, etc. In this regard, LDHs can be applied as a sonophotocatalyst because of their exceptional catalytic properties. As a cost-efficient catalyst, LDHs have been widely studied due to their large surface area, simple synthesis procedure, and unique structure [23]. Along with aluminum, magnesium, and iron, various LDHs containing other layered cationic metals such as zinc, cobalt, calcium, manganese, nickel, and copper have been incorporated into LDHs lattice [24]. Specifically, LDHs which contain Cu are vastly utilized in diverse catalytic fields due to the specific structure and the acceptable catalytic activity of the Cu atom [25]. LDHs are also recognized as functional materials that have antimicrobial properties. Taking this idea into consideration, Mishra et al. reported the high antibacterial activity of Cu substituted Zn Al LDH against both gram-negative (*E. coli*) and gram-positive (*S. aureus*) species [26]. Also, selenium doped Ni-Ti LDH, which was developed by Wang et al. can efficiently hinder the growth of *S. aureus* and *Escherichia coli* (*E. coli*) [27].

In this study, two tri-metal LDHs (FeCuMg and CrCuMg) were utilized as sonophotocatalyst for the catalytic degradation of a model organic dye. Sonocatalysis in the presence of a suitable catalyst is also considered as an efficient method for the treatment of

wastewaters contaminated with dyes. Hence, LDHs are applied as sonocatalysts for the generation of $\cdot\text{OH}$ under ultrasonication [28]. In the present study, the photocatalytic degradation of the target organic dye was performed under ultrasonication, named sonophotocatalysis, to achieve the maximum decolorization efficiency at low reaction time. In fact, both light source (LED lamp) and ultrasound were implemented to stimulate tri-metal LDHs for the maximum generation of $\cdot\text{OH}$ in the aqueous matrix. It is demonstrated that the combination of ultrasound (sonolysis) and photocatalysis (sonophotocatalysis) has higher efficiency than that of the individual processes of sonolysis, photolysis, sonocatalysis, and photocatalysis [17, 29]. Tri-metal LDHs were synthesized through a facile hydrothermal method. A comprehensive comparison was performed along with the evaluation of the effect of main operational parameters on the efficiency of the applied processes. The main intermediate byproducts generated during the sonophotocatalytic process were identified. The above-mentioned systems based on the application of Fe and Cr-incorporated LDHs have not been investigated before in the literature. Interestingly, we uncover the antibacterial behaviors of the synthesized LDHs against *S.aureus*. To the best of our knowledge, based on an extensive literature review, CrCuMg and FeCuMg LDHs with antibacterial functionality have not been reported so far.

2. Materials and methods

2.1. Materials

All the reagents were procured from Merck Co., which were of analytical grade and utilized without additional purification. Acid blue 113 was purchased from Shimi Boyakhsaz Co. (Iran). Nutrient agar and nutrient broth were provided by Biomark Laboratories (India).

2.2. Synthesis of FeCuMg and CrCuMg LDHs

The FeCuMg and CrCuMg LDHs were prepared by the hydrothermal method. The synthesis method was carried out as follows: a solution of NaOH (4 mol L^{-1}) was transferred dropwise into a solution including $0.05 \text{ mol Cu(NO}_3)_2 \cdot 6\text{H}_2\text{O}$, $0.10 \text{ mol Mg(NO}_3)_2 \cdot 6\text{H}_2\text{O}$ and 0.05 mol of $\text{Fe(NO}_3)_3 \cdot 9\text{H}_2\text{O}$ or $\text{Cr(NO}_3)_3 \cdot 9\text{H}_2\text{O}$ (the molar ratio of Cr/Mg/Cu and Fe/Mg/Cu is 1:2:1) and stirred vigorously under the argon atmosphere at $65 \text{ }^\circ\text{C}$ until the ultimate pH of 8.5–9.0 reached. Afterward, the final suspension was inserted into a stainless steel autoclave and remained for 24 h at $120 \text{ }^\circ\text{C}$. The synthesized sample was washed and centrifuged with ethanol and deionized water up to pH = 7. At last, the catalyst was dried in an oven ($85 \text{ }^\circ\text{C}$) for 18 h and grounded.

2.3. Characterization instruments

To specify the crystallographic characterization of the samples, X-ray diffraction (XRD) analysis (D8 Advance, Bruker, Germany) with the Cu $K\alpha$ radiation of 0.15406 nm at 40 mA and 45 kV was applied. Tescan Mira3 microscope (Czech Republic) was used to record the scanning electron microscopic (SEM) images and energy-dispersive X-ray (EDX) spectroscopy of the samples. To measure the bandgap of the synthesized LDHs, UV-Vis diffuse reflectance spectrophotometer (DRS) spectra were evaluated on an Analytik Jena spectrophotometer (S 250, Germany). To investigate the chemical oxidation state and the elemental composition of the samples, X-ray photoelectron spectroscopy (XPS) measurements were operated through a spectrometer (Kratos AXIS UltraDLD, UK). The infrared spectra of the samples were conducted on a Fourier transform infrared spectroscopy (FTIR, Bruker Tensor 27, Germany). High-resolution transmission electron microscopy (HRTEM) was done by JEM-2100, Jeol (Japan). The surface parameters of the samples were studied by Brunauer-Emmett-Teller (BET) analysis via Belsorp Mini II (Japan). The photoluminescence (PL)

spectra of the LDHs were analyzed by a spectrometer (Perkin Elmer LS45, USA). Gas chromatography-mass spectrometry (GC-MS) was used to determine the intermediate by-products produced during AB113 degradation.

2.4. Sonophotocatalytic experiments

The decolorization efficiency of AB113 was evaluated by an ultrasound bath (Ultra 8060, 150 W, 36 kHz, England) and in the presence of a LED lamp. The wattage, wavelength, and the light intensity of the LED lamp were 10 W, ~400 nm and 79.62 W m^{-2} , respectively. A pyrex Erlenmeyer flask containing the dye solution (100 mL) with the predetermined amount of the catalyst was immersed at 2/3 of its height inside the ultrasonic bath and the LED lamp located at the 10 cm above the Erlenmeyer. They were maintained at the same position in all the tests to confirm sufficient reproducibility. The pH of the prepared solution was controlled with a pH meter (Ohaus 3100, USA) by adding either HCl or NaOH. Before the treatment process, the AB113 solution was stirred in the dark for 30 min to reach the adsorption equilibrium. Afterward, the solution was kept in the ultrasound bath for 60 min at room temperature. Within the process, 3 mL of the solution was withdrawn at 10 min intervals. The absorbance of the AB113 was measured using a spectrophotometer (SU-6100, Philler scientific, USA). The decolorization efficiency (DE%) was calculated via $DE(\%) = \frac{C_0 - C_t}{C_0} \times 100$ in which C_0 and C_t were the initial concentration and concentration of organic dye at a specified time, respectively. The ultrasonic energy expended into the solution was obtained using a calorimetric analysis according to $P = \left(\frac{dT}{dt}\right) \times c_p \times M$ in which P is the power (W), c_p is the heat capacity of water (4.2 J g^{-1}) and M is the mass of water (g). $\left(\frac{dT}{dt}\right)$ is the linear slope of the thermometer rise during the different time intervals (K s^{-1}).

2.5. Antibacterial activity test

Staphylococcus aureus ATCC 25993 was cultured in nutrient broth and incubated at 37 °C overnight till an optical density at 600 nm (OD600) of 0.5 was obtained. The antibacterial activities of the as-prepared LDHs were evaluated against *S. aureus*, as a Gram-positive bacteria. 1.5 mL of the catalyst suspensions were prepared with the different concentrations of 400 and 600 $\mu\text{g mL}^{-1}$ with 200 μL of *S. aureus* cultures (10^5 colony-forming unit (CFU)). The LDH and bacteria suspensions and the control sample were located in the shaker for 2 h (37 °C and 200 rpm shaking speed). Then 50 μL of the samples were spread onto nutrient agar plates and maintained to grow overnight (37 °C). The remained bacterial colonies were counted. The bactericidal rates were computed by Loss of viability = $(1 - N_2/N_1) \times 100$, in which N_2 and N_1 are the numbers of the grown colonies exposed to LDHs and control solutions, respectively.

The minimum inhibitory concentration (MIC) and minimum bactericidal concentration (MBC) of the CrCuMg and FeCuMg LDHs were tested in 96-well microplates. 100 μL of LB broth was added to all wells except wells in column 1. Afterward, 100 μL of the as-synthesized catalysts ($800 \mu\text{g L}^{-1}$) were inserted into the wells of columns 1 and 2. All wells were homogenized and 100 $\mu\text{L well}^{-1}$ was moved from column 2 to column 3 wells and repeated up to column 11. Then, 10 μL of *S. aureus* (10^3 CFU mL^{-1}) was transferred to the entire wells except for columns 11 and 1. In addition, the *S. aureus* (10 μL) was inserted into column 12 as a control sample too. The microplates were incubated (37 °C, 24 h). The lowest concentration of LDHs with no obvious bacterial growth detected is defined as the MIC value. Also, MBC is described as the least concentration of the antibacterial agent needed to kill microorganisms. The transparent wells were cultured in nutrient agar plate to introduce MIC and MBC values.

3. Results and discussion

3.1. Characterization of the synthesized LDHs

The results of SEM analysis are provided in Fig. 1. Based on the obtained images, it can be stated that the hydrothermal synthesis of both FeCuMg LDH (Fig. 1a and b) and CrCuMg LDH (Fig. 1c and d) led to the formation of nanostructures with significant reaction sites for the catalytic degradation of AB113. The SEM images showed that the as-synthesized LDHs have a flower-like shape with lamellar structures. The finest details of the internal structure of the as-synthesized LDHs are shown in HRTEM images (Fig. 2). The features of FeCuMg LDH (Fig. 2a) and CrCuMg LDH (Fig. 2b), including dislocations, grain boundaries, and crystalline structure can be evidently seen through HRTEM images. The growth of layered structure and defects in the structure of LDHs are observable. The bright and dark parts in the HRTEM images indicate the ionic parts and hydroxide layers of the LDH, respectively [30].

< Fig. 1 >

< Fig. 2 >

The pore volume data and specific surface area of both FeCuMg and CrCuMg LDHs are specified in Table 1. Based on the BET plot, the specific surface area of FeCuMg and CrCuMg LDHs was obtained to be 1.65 and 2.20 m² g⁻¹, respectively, indicating a higher surface area of Cr-incorporated LDH in comparison with Fe-incorporated LDH. This could be beneficial for the enhanced sonophotocatalytic degradation of AB113 over LDH. The high surface area provides more adsorptive sites with high ability towards the target contaminant, generating photo-induced electron/hole pairs on the available active sites [31]. The results of the Langmuir plot confirmed the BET plot data. According to the BET data, the V_m of CrCuMg LDH (0.50 cm³ (STP) g⁻¹) was higher than that of FeCuMg LDH (0.38 cm³ (STP) g⁻¹) which exhibited the high porosity of the CrCuMg LDH sample compared with the Fe-contained layered material. The high porosity of the layered catalysts is favorable for the diffusion and transportation of the species [31].

Table 1. Pore volume data and specific surface area of both FeCuMg and CrCuMg LDHs based on different plots.

Plots	Variables	FeCuMg LDH	CrCuMg LDH
BET plot	V_m [$\text{cm}^3(\text{STP}) \text{g}^{-1}$]	0.38	0.50
	a_s , BET [$\text{m}^2 \text{g}^{-1}$]	1.65	2.20
	C	247.24	389.36
	Total pore volume($p/p_0=0.990$) [$\text{cm}^3 \text{g}^{-1}$]	0.0041	0.0041
	Mean pore diameter [nm]	10.02	7.50
Langmuir plot	V_m [$\text{cm}^3(\text{STP}) \text{g}^{-1}$]	0.70	0.64
	a_s , Lang [$\text{m}^2 \text{g}^{-1}$]	3.03	2.77
	B	0.066	0.12
t plot	a_1 [$\text{m}^2 \text{g}^{-1}$]	0.50	0.73
	V_1 [$\text{cm}^3 \text{g}^{-1}$]	0.00	0.00
BJH plot	V_p [$\text{cm}^3 \text{g}^{-1}$]	0.0047	0.0045
	$r_{p,\text{peak}}$ (Area) [nm]	1.22	1.22
	a_p [$\text{m}^2 \text{g}^{-1}$]	4.00	3.99

The EDX micrographs of FeCuMg LDH (Fig. 3a) and CrCuMg LDH (Fig. 3b) were taken based on the results of SEM analysis to specify and quantify the elements in the structure of layered materials. In the case of FeCuMg LDH sample, O, Fe, Cu, N, and Mg elements were detected with a weight percentage of 44.57, 27.22, 22.92, 3.57, and 1.72%, respectively. For CrCuMg LDH, O, Cu, Cr, N, and Mg were specified with a weight percentage of 57.09, 15.19, 12.81, 10.84, and 4.07%, respectively.

The XRD patterns of LDH samples were taken and depicted in Fig. 3c. The results of both FeCuMg LDH and CrCuMg LDH indicated the crystalline structure of the as-synthesized samples. The obtained patterns exhibited the diffraction peaks of the LDHs lattice through a hexagonal phase. In both patterns, the peaks placed at 10.54° , 20.19° , 27.09° , 29.69° , 35.44° , 39.14° , and 60.04° were indexed to the (003), (006), (101), (009), (015), (018), and (113) planes, respectively, corresponding to the hydroxalcalite structure of the samples [32]. The obtained peaks are in accordance with the hexagonal phase of the LDH structure. In addition,

sharp peaks appearing in the pattern of CrCuMg LDH confirm that CrCuMg LDH has a better crystallinity comparing with FeCuMg LDH.

The FT-IR spectra of LDH samples showed the presence of various functional groups in the structure of LDHs (Fig. 3d). Since catalytic reactions take place on the surface, the presence of various surface functional groups on the surface of LDHs leads to the enhanced efficiency of the treatment process. Moreover, functional groups play a major role in the incorporation of metals into the layered structure. According to Fig. 3d, the broad peak centered at 3420 cm^{-1} is attributed to the stretching vibrations of hydroxyl groups ($-\text{OH}$) from metal-hydroxyl bonds in the layers and interlayer hydrogen-bonded water molecules [15, 33]. The peak shows the superposition of stretching hydroxyl $\nu(\text{OH}_{\text{str}})$ due to metal-hydroxyl band in the layered material and interlayer water molecules with hydrogen binding [34]. This sharp peak disappeared in the surface structure of CrCuMg LDH, indicating that Cr is effectively intercalated in the LDH lattice. The absorptive band placed at 1643 cm^{-1} is associated with water deformation $\delta(\text{H}_2\text{O})$ [34]. The band at 1390 cm^{-1} is attributed to the asymmetric stretching of the carbonate (CO_3^{2-}) anions in the interlayer of the LDH structure [35]. The peaks at 835 and 609 correspond to the lattice vibration of metal-O-H and metal-O, respectively [6].

XPS analysis was also performed and the obtained spectra were illustrated in Fig. 3e and f. Fig. 3e shows the spectrum of Fe-incorporated LDH exhibiting the surface chemistry of the layered material. The presence of Fe, Cr, Cu, and Mg were analyzed based on the obtained survey scans, which were in good consistency with the EDX results. The binding energy in the range of 0-1200 eV (full-range XPS spectrum) was implemented for scanning. In the case of the spectrum of Fe-intercalated LDH (see Fig. 3e and Fig. S1), two peaks of Fe $2p_{3/2}$ and Fe $2p_{1/2}$ are placed at $\sim 709\text{-}715$ and $\sim 724\text{-}729$ eV, respectively, exhibiting the co-existence of Fe^{2+} and Fe^{3+} in the structure of FeCuMg-LDH [36]. The satellite peaks (two peaks at both

sides of the Fe 2p_{1/2}) are generated by configuration interaction which is arisen from the relaxation of the valence electrons in Fe³⁺ at 2p state.

As illustrated in Fig. 3f and Fig. S2, the two strong peaks of Cr 2p_{3/2} (577-580 eV) and Cr 2p_{1/2} (586-589 eV) are ascribed to trivalent chromium (Cr³⁺) in the structure of Cr-incorporated LDH. As illustrated in Figs 3e, 3f, S1, and S2, the Cu 2p regions have Cu 2p_{1/2} peaks at about 953-957 eV and 961-965 eV, and Cu 2p_{3/2} peaks at 931-937 eV and 940-945 eV, respectively, confirming that the divalent and univalent copper present on the surface. As expected, the XPS analyses of the Mg 2p spectra indicate that the peak at 49.5 eV related to Mg(OH)₂ and the peak at about 51 eV corresponded to MgO. For both sonophotocatalysts, the main O 1s peak located at about 530 eV proved the presence of several oxygen species on the surface of the as-synthesized sonophotocatalysts with different chemical structures. In fact, the O 1s peak with high binding energy is associated with losing oxygen species bounded on the surface of layered compounds (O_{ads}) [37]. The C 1s spectra for both FeCuMg and CrCuMg LDHs are displayed in Figs. S1 and S2, representing the environment hydrocarbons and CO₃²⁻.

< Fig. 3 >

< Fig. S1 >

< Fig. S2 >

3.2. The comparison of different processes for the removal of AB113

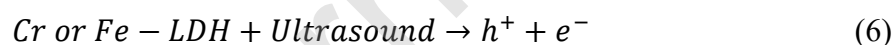
For both sonophotocatalysts of FeCuMg LDH and CrCuMg LDH, a comparative study was performed to specify the role of the individual processes of sonolysis, photolysis, sonophotolysis, sonocatalysis, photocatalysis and finally sonophotocatalysis in the removal of AB113 (Figs. 4a and b). This set of examinations was performed within the contact time of 60 min at a pH value of 8.0. Moreover, the contribution of the adsorption process to the removal of the target pollutant was also determined. The adsorption process of AB113 on the surface of

both FeCuMg LDH and CrCuMg LDH with the same dosage of 0.5 g L⁻¹ was not efficient enough for the decolorization of the aqueous solution containing 50 mg L⁻¹ of AB113 (the removal efficiency of 19.0% for FeCuMg LDH and 35.1% for CrCuMg LDH). According to the results, the role of ultrasound alone (sonolysis: 13.0%) and LED lamp alone (photolysis: 13.5%) was insignificant in the removal of AB113 from the aquatic phase. The insignificant photodegradation (photolysis alone) of organic pollutants under visible light irradiation has been reported [38]. Apparently, the visible light irradiation is not powerful enough to break the chemical bonds of the model organic pollutant in the absence of an appropriate photocatalyst [39]. The implementation of ultrasound brings about the formation of $\cdot\text{OH}$ and other oxidizing agents such as hydrogen peroxide in the liquid stream as represented in the following equations [16, 40]:



However, the utilization of ultrasound alone leads to the production of the limited number of oxidizing agents in the aquatic phase. The combination of sonolysis (ultrasonic power of 150 W) with photolysis (10W LED lamp) named sonophotolysis was also inefficient for the degradation of AB113 in 60 min (24.5%). The photocatalysis, sonocatalysis, and sonophotocatalysis of AB113 over FeCuMg LDH led to the decomposition efficiency of 27.5, 42.4, 57.3%, respectively, while in the case of CrCuMg LDH catalyst, the efficiencies of photocatalysis, sonocatalysis, and sonophotocatalysis were obtained to be 47.9, 65.4, 81.1%,

respectively. As obtained from the experiment, the presence of LDHs (both FeCuMg and CrCuMg LDHs) enhanced the degradation efficiency of AB113 due to their catalytic activity. Layered materials containing transition metal cations act as a photocatalyst for the decontamination of water since they provide spatially segregated oxidation and reduction reactive sites [10]. In fact, metals (Cr and Fe) intercalated in the structure of LDHs serve as doping agents for the visible light-responsive photocatalytic degradation of organic molecules [31]. The increase in the sonophotocatalytic activity of layered compounds in comparison with the photocatalysis and sonocatalysis is due to the combination of the direct process of $\cdot\text{OH}$ generation with its indirect generation by the inspiration of the holes (reaction with $\text{H}_2\text{O}/\text{OH}^-$ as electron donor molecules), thereby producing the more amounts of $\cdot\text{OH}$ reactive radicals in the sonophotocatalytic process (Eqs. 6-8) [41, 42]. During the sonophotocatalysis over LDHs, ultrasound (US) aids the reduction of electrons/holes recombination rate for the enhanced generation of $\cdot\text{OH}$. Extra amounts of $\cdot\text{OH}$ radicals are generated via emission of photons by sonoluminescence (SL) phenomenon of the sonocatalytic process as well as by the deaggregation of fine particles of the layered sonocatalyst in the solution [43]. Moreover, the interaction between the water molecules adsorbed onto LDHs and the holes generated via the SL phenomenon produces more $\cdot\text{OH}$ radicals in the reactor [36]:



The superior destructive decolorization ability of the sonophotocatalysis compared with the photocatalysis and sonocatalysis is in accordance with the reported literature data [39]. According to the obtained data, the sonocatalytic activity of both FeCuMg LDH and CrCuMg LDH was higher than photocatalytic activity regarding the degradation of the model organic

pollutant of AB113. This can be attributed to the presence of Cu ions in the structure of as-prepared layered catalysts improving the adsorption of emitted photons from the SL phenomenon generating more electron-hole pairs in the bulk solution for the formation of hydroxyl radicals as well as the enhanced nucleation of micro-bubbles during cavitation phenomenon [44]. On the whole, CrCuMg LDH was more efficient than FeCuMg LDH to generate $\cdot\text{OH}$ due to the simultaneous ultrasonication and visible light radiation, enhancing the degradation of AB113 in the liquid phase. The implementation of tri-metal-contained layered materials as sonocatalyst provides more nuclei to form cavitation bubbles in the solution for the enhanced pyrolysis of water molecules, elevating the generation of $\cdot\text{OH}$. The SL phenomenon and formation of electron/hole pairs due to the presence of a suitable layered catalyst under visible light irradiation can also be expected for the production of extra $\cdot\text{OH}$ in the solution [45].

In fact, the unique structure of LDH promotes the absorption of visible light irradiation in the solution as well as ultrasonic irradiation. Since the SL phenomenon is one of the main mechanisms governing the degradation of the target pollutant, it can be concluded that the bandgap energy of as-synthesized layered catalysts plays a remarkable role in sonophotocatalysis performance. The values of bandgap energy are obtained for each catalyst by using the Tauc's equation and plotting $(\alpha h\nu)^2$ versus the photon energy ($h\nu$) (Figs. 4c and d) [46].

< Fig. 4 >

Accordingly, the bandgap energy of FeCuMg LDH and CrCuMg LDH was found to be 2.54 and 2.41 eV, respectively, suggesting the higher photocatalytic activity of Cr-incorporated LDH in comparison with the FeCuMg LDH. It is demonstrated that the incorporation of photo-active metal components such as Zn, Ti, Fe, or Cr into LDHs can provide transition metal-

contained LDHs as efficient semiconductors with bandgap energy in the range of 2.0-3.4 eV [10]. The lower bandgap energy of CrCuMg LDH compared with FeCuMg LDH suggests that lower energy is required to excite electrons which are generated via the “sonoluminescence” phenomenon. Moreover, Table 2 compares the application of the different LDHs which have been utilized for the degradation of organic pollutants.

Table 2 evaluates the results of the present study along with the other similar papers which confirms that the CrCuMg LDH can be considered as a suitable catalyst for the degradation of other organic contaminants by the different AOPs. It should be mentioned that the chemical structure of AB113 is more complicated ($C_{32}H_{21}N_5Na_2O_6S_2$, with 6 aromatic rings and double azo groups) in comparison with the other pollutants in Table 2. So, it is difficult to degrade and mineralize these kinds of refractory compounds. Moreover, the concentration of the pollutant in the present study is 50 mg L^{-1} which is degraded within 60 min of the sonophotocatalytic process and in the presence of 0.5 g L^{-1} of the catalyst. So, it can be deduced that 81.1 % of degradation efficiency is achieved in the presence of the low catalyst dosage, the high concentration of AB113, and low time which can be considered as the advantages of the present study.

Table 2. The degradation of organic pollutants in the presence of LDHs via AOPs.

LDH	Pollutant	Catalyst dosage (g L^{-1})	Time (min)	AOP method	DE (%)	Ref.
CuMgFe	Ethylbenzene (8.49 mg L^{-1})	0.2	1440	Persulfate activation	93.7	[47]
CuZnTi	Methylene blue (10 mg L^{-1})	0.5	90	Sonocatalysis	71	[44]
NiZnAl	Orange G (50 mg L^{-1})	0.5	100	Photocatalysis	99	[48]
PtZnTi	Rhodamine B (10 mg L^{-1})	1	12	Photocatalysis	100	[49]

CrCuMg	AB113 (50 mg L ⁻¹)	0.5	60	Sonophotocatalysis	81.1	Present study
--------	--------------------------------	-----	----	--------------------	------	---------------

3.3. Operational parameters

3.3.1. Pollutant concentration

The effect of the initial concentration of AB113 on its removal by the sonophotocatalytic process was studied by varying the initial concentration in the range of 40-70 mg L⁻¹. Based on Fig. 5, increasing the initial concentration of AB113 from 40 to 70 mg L⁻¹ resulted in decreasing the efficiency of sonophotocatalytic process from 66.0 to 31.0% and 88.9% to 47.5% when FeCuMg LDH (Fig. 5a) and CrCuMg LDH (Fig. 5b) were used as a sonophotocatalyst, respectively. Obviously, increasing target pollutant concentration leads to the decreased efficiency of the treatment process because of the higher amounts of oxidative agents required for the decomposition of more target molecules. On the other hand, as the initial concentration of AB113 increases, the number of existing $\cdot\text{OH}$ generated through the sonophotocatalysis is not adequate to decompose the high concentrations of the target pollutant, leading to diminished decomposition efficiency [50]. Therefore, at the same operational conditions, the decreased efficiency of the sonophotocatalytic process over both FeCuMg LDH and CrCuMg LDH with increasing the initial AB113 concentration is inevitable.

< Fig. 5 >

3.3.2. Sonophotocatalyst dosage

The dosage of sonophotocatalysts was varied in the range of 0.1-1.0 g L⁻¹ to evaluate the influence of this main parameter on the effectiveness of the treatment process (Fig. 6). In the case of FeCuMg LDH (Fig. 6a), the results showed the increased efficiency of AB113 degradation from 35.5 to 65.2% with increasing the dosage from 0.1 to 0.7 g L⁻¹, while

increasing the dosage to 1.0 g L^{-1} led to a remarkable decrease in the degradation efficiency (52.1%). For CrCuMg LDH, increasing the efficiency from 40.7 to 81.1% was observed when the dosage increased from 0.1 to 0.5 g L^{-1} , respectively (Fig. 6b). Notably, a substantial reduction in the degradation efficiency of AB113 (about 30% reduction in the efficiency) was observed when the CrCuMg LDH dosage of 1.0 g L^{-1} was implemented. Increasing the amount of LDHs provides more nuclei for the formation of $\cdot\text{OH}$ [43]; however, the higher dosage of Fe and Cr-incorporated LDHs increases the turbidity of the bulk solution, thereby hindering the transmittance of visible light through the solution. Furthermore, the higher dosage of the layered catalyst is not required due to the high potential of aggregation in the liquid phase [51]. Thus, the determination of the optimum dosage of the applied sonophotocatalyst is essential for conducting a cost-efficient treatment process with high potential to be utilized in the full-scale operation.

< Fig. 6 >

3.3.3. Initial pH and pH_{pzc}

The efficiency of both Fe and Cr-incorporated LDHs as a sonophotocatalyst for the degradation of AB113 was evaluated under different pH values. According to the results provided in Figs. 7a and c, the AB113-contained solution with the initial pH of 8.0 caused the highest sonophotocatalytic degradation of AB113 for both FeCuMg LDH (57.3%) and CrCuMg LDH (81.1%). The decolorization efficiency of the AB113-contained solution by the treatment process gradually increased with increasing the initial pH value from 4.0 to 8.0, achieving the best result at an initial pH of 8.0. Increasing the initial pH to the basic value of 13.0 and its decrease to the acidic values of 6.0 and 4.0 resulted in a significant decrease in the sonophotocatalytic degradation efficiency of AB113. The minimum degradation efficiency of AB113 was observed at a basic pH value of 13.0 for both Fe and Cr-incorporated layered

sonophotocatalysts. The various surface complexes of hydroxyl ions are formed due to the larger number of hydroxyl anions at basic conditions, impeding the direct interaction between the sonophotocatalysts and the exciting agents such as ultrasound and visible light, resulting in lower degradation efficiency [52].

The surface charge of the layered catalyst is susceptible to pH variations, thereby affecting the process performance [53]. Thus, the point of the zero charges (pH_{pzc}) of the sonophotocatalysts was determined through the pH drift method. Accordingly, the values of pH_{pzc} for FeCuMg LDH (Fig. 7b) and CrCuMg LDH (Fig. 7d) were obtained to be 8.7 and 7.5, respectively. Thus, the surface of the layered sonophotocatalyst is protonated at $\text{pH} < \text{pH}_{\text{pzc}}$, while it is deprotonated (negative charge) at $\text{pH} > \text{pH}_{\text{pzc}}$. Conclusively, the diminished degradation efficiency of AB113 at a strong basic pH of 13.0 is attributed to the increased electrostatic repulsion between the anionic dye and negatively charged surface of the studied sonophotocatalysts. On the other hand, under basic conditions, the presence of excessive amounts of hydroxyl ions prevents the surface adsorption of anionic dyes by the adsorbent, resulting in decreased adsorption capacity [15, 53]. The surface adsorption of the target pollutant on the sonocatalyst plays a major role during the sonocatalysis over layered sonocatalysts. In the case of both layered compounds, the diminished degradation efficiency of AB113 at strong acidic pH conditions (pH: 4.0) may be associated with the corrosion of sonocatalyst under high hydrogen ions concentrations [28].

< Fig. 7 >

3.3.4. Ultrasound power

The ultrasound power was set at 150, 200, and 300 W to assess its effect on the degradation efficiency of AB113 where some other parameters were kept constant within the reaction time of 60 min. The sonophotocatalytic reactor contained 50 mg L⁻¹ of AB113 radicals at an initial

pH of 8.0 in the presence of 0.5 g L^{-1} of sonophotocatalyst. The results are exhibited in Fig. 8. When the FeCuMg LDH was used, increasing the power from 150 to 300 W had no significant effect on the degradation efficiency of AB113 (increasing from 57.3 to 66.8%). Similar results were observed when CrCuMg LDH was used as the sonophotocatalyst. A two-fold increase in the ultrasound power (from 150 to 300 W) led to a lower than 10% increase in the degradation efficiency. For this reason, the ultrasound power of 150 W was chosen for performing the experimental runs of the present investigation. The increased number of cavitation bubbles is predictable due to the hot spot mechanism at the high power of ultrasound [40]. However, the high power of ultrasound increases the turbulence of the LDH-contained solution, preventing the effective transmittance of light irradiation in the bulk solution for the photocatalysis of AB113. It should be noted that the real ultrasonic powers, which were dissipated in the solution measured by the calorimetric method are 1.38, 1.67, and 3.47 W for 150, 200, and 300 W, respectively.

< Fig. 8 >

3.4. The presence of radical scavengers

The presence of various radical scavengers and their effect on the sonophotocatalysis of AB113 were investigated to evaluate the effectiveness of the treatment process under adverse conditions that may exist in real industrial wastewaters. Moreover, it is well known that $\cdot\text{OH}$ and $\text{O}_2^{\cdot-}$ radicals, along with the photo-generated holes (h^+) are the main oxidizing agents for the degradation of organic target pollutants. Therefore, the possible degradation mechanism and chemical species responsible for the degradation of AB113 can be specified by the addition of appropriate quenchers for the aforementioned active species. For this purpose, parabenzoquinone ($\text{O}_2^{\cdot-}$ scavenger) [54], formic acid (hole scavenger) [55], and isopropanol ($\cdot\text{OH}$ scavenger) [42] with two different molar ratios (1:1 and 1:10) were added to the AB113-

contained solution (Fig. 9). For the sonophotocatalysis of AB113 over FeCuMg LDH, the presence of parabenzoquinone, formic acid and isopropanol with the molar ratio of 1:1 led to a decrease in the efficiency of the process from 57.3 to 53.0, 37.2 and 28.8%, respectively (Fig. 9a-1). At a molar ratio of 1:10, the efficiency of the FeCuMg LDH-contained treatment process decreased to 46.8, 29.1, and 21.7%, respectively (Fig. 9b-1). It can be concluded that the presence of isopropanol causes the most inhibiting effect on the sonophotocatalytic conversion of AB113. Moreover, the addition of radical scavengers with a molar ratio of 1:10 resulted in a more inhibiting effect than that of 1:1. Similar trends were observed when CrCuMg LDH was implemented as sonophotocatalyst. The presence of parabenzoquinone, formic acid, and isopropanol with a molar ratio of 1:1 led to decreasing the efficiency of the process from 81.1 to 57.0, 37.1, and 34.4%, respectively (Fig. 9a-2). At a molar ratio of 1:10, the efficiency of the CrCuMg LDH-contained treatment reactor decreased to 54.0, 33.9, and 29.9%, respectively (Fig. 9b-2). The addition of isopropanol as an alcoholic compound with $\cdot\text{OH}$ radical scavenging characteristics caused the most suppressing effect on the sonophotocatalysis of AB113 over both FeCuMg LDH and FeCuMg LDH; thus, the decomposition of AB113 can be mainly ascribed to the formation of $\cdot\text{OH}$ in the liquid phase. Isopropanol is generally used as a quenching agent for both sulfate and hydroxyl radicals [56]; however, the generation of sulfate-free radical in the present study is not expected.

< Fig. 9 >

Photoluminescence (PL) analysis with the terephthalic acid solution was carried out at different time intervals. As can be observed from Fig. S3, the PL spectra changed during the sonophotocatalytic process in the presence of FeCuMg LDH (Fig. S3a) and CrCuMg LDH (Fig. S3b) at different time intervals. By increasing the time of the process, the production of hydroxyl radicals is promoted, confirming the generation of hydroxyl radicals during the sonophotocatalytic process and its main impact on degradation efficiency.

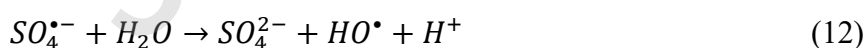
< Fig. S3 >

3.5. The presence of radical enhancers

Two main radical enhancers, including hydrogen peroxide and potassium persulfate, were added to the sonophotocatalytic reactor to enhance the efficiency of the process regarding the decolorization of AB113 (Fig. 10). The enhanced sonophotocatalytic degradation of AB113 over FeCuMg LDH from 57.3 to 59.2 and 76.6% was obtained in the presence of hydrogen peroxide and potassium persulfate, respectively (Fig. 10a). The addition of hydrogen peroxide (3.0% increase) and potassium persulfate (more than 8.0% increase) led to an insignificant increase in the sonophotocatalysis of AB113 over CrCuMg LDH (Fig. 10b). The insignificant influence of hydrogen peroxide may be associated with its simultaneous radical enhancing and radical scavenging properties as exhibited in Eqs (9 and 10) [43]:



In general, the addition of potassium persulfate brought about more enhancing effect than that of hydrogen peroxide, especially in the case of the application of FeCuMg LDH as the sonophotocatalyst. Up to 20.0% increase in the efficiency of the FeCuMg LDH-contained treatment system was achieved when potassium persulfate was added to the reactor according to the following equations:



The reduced recombination rate of electron/hole pairs as well as the enhanced creation of $\cdot\text{OH}$ and $\text{SO}_4^{\cdot-}$ can be expected due to the addition of persulfate ions as shown in the abovementioned relations [40, 56].

< Fig. 10 >

3.6. Reusability and stability tests

The reusability potential of the layered sonophotocatalysts was evaluated to exhibit the applicability of the as-synthesized sonophotocatalyst in full-scale operation. Five consecutive experimental runs were performed; the decolorization efficiency of AB113 was recorded at the end of each run (Fig. 11). According to Fig. 11a, about 19% reduction in the sonophotocatalytic decolorization of AB113 was observed after the fifth run when FeCuMg LDH was implemented as sonophotocatalyst. As can be seen in Fig. 11b, a similar result was obtained when CrCuMg LDH was used as the sonophotocatalyst. LDHs as the heterogeneous catalysts with solid base are promising catalysts considering economical and environmental viewpoints. Because unlike homogeneous catalysts, LDHs are recyclable catalysts for the several types of destructive reactions within repeated experimental runs [10]. Eshaq and ElMetwally have demonstrated the high reusability potential of metal-incorporated LDHs. They found that the structure of MgZnAl LDH survives even after reusing the catalyst within four operational runs [57]. Due to their unique layered structure, high stability and recyclability of LDHs have been observed in the catalytic treatment systems [58].

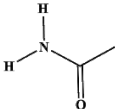
< Fig. 11 >

3.7. Intermediate byproducts

The intermediate byproducts generated during the sonophotocatalysis of AB113 by both Fe- and Cr-intercalated LDHs were identified using GC-MS analysis. Accordingly, the

intermediate byproducts of AB113 generated during its sonophotocatalysis over FeCuMg LDH and CrCuMg LDHs are listed in Tables 3 and 4, respectively. Five main byproducts were identified when FeCuMg LDH was used for the sonophotocatalysis of AB113, indicating significant progress in the mineralization of AB113 during the sonophotocatalysis. Moreover, some other by-products may be formed that were not recognized. Similarly, some intermediates with the simpler structure and lower molecular weight were identified in the case of the utilization of CrCuMg LDH as the sonophotocatalyst. The first step of the degradation can be assumed to be the cleavage of the bonds of C–C, C–N, and C–S. Then, the decomposition of some rings resulted in the generation of the aromatic and aliphatic compounds, including N heteroatom. According to the intermediates listed in Tables 3 and 4, some hydroxylated intermediates are produced during the degradation of AB113, indicating that the decomposition of AB113 over tri-metal LDHs initiates with the attack of hydroxyl radical [39]. These results were in accordance with the PL analyses and the obtained data when radical scavenging compounds were added to the sonophotocatalytic reactor. Subsequently, cleavage of the rings by consecutive attacks of ROSs can cause the generation of aliphatic compounds with low-carbon-level. Ultimately, some of these aliphatic compounds can be partially mineralized into acetic acid, inorganic ions, CO₂, and H₂O.

Table 3. Identified byproducts generated during sonophotocatalytic degradation of AB113. ([AB113]₀ = 50 mg L⁻¹, [FeCuMg LDH] = 0.5 g L⁻¹, ultrasound power = 150 W and pH = 8).

No.	Compound name	Structure	t _R (min)	Main fragments (m/z)/(percent)
1	Cyclobutanone		2.152	73.00 (100 %), 101.00 (54.77 %), 55.00 (41.11 %), 103.00 (31.56 %), 57.10 (28.68 %)
2	Ethanamide		4.238	75.00 (100 %), 116.00 (94.83 %), 73.00 (13.47 %), 117.00 (10.52 %), 76.00 (8.11 %)

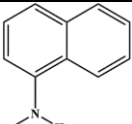
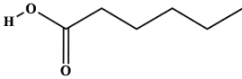
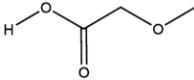
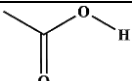
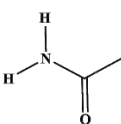
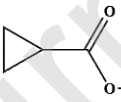
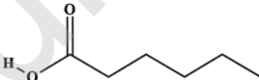
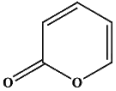
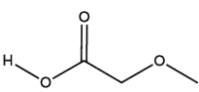
3	1-Naphthylamine		26.154	171.00 (100 %), 154.90 (51.46 %), 283.10 (8.75 %), 172.00 (8.66 %), 57.00 (7.76 %)
4	Hexanoic acid		30.692	99.00 (100 %), 57.00 (37.54 %), 113.00 (26.45 %), 71.10 (25.46 %), 55.00 (22.66 %)
5	Methoxy acetic acid		34.154	57.10 (100 %), 207.00 (77.52 %), 55.00 (66.64 %), 71.10 (66.40 %), 69.00 (51.56 %)

Table 4. Identified by-products generated during sonophotocatalytic degradation of AB113.

([AB113]₀ = 50 mg L⁻¹, [CrCuMg LDH] = 0.5 g L⁻¹, ultrasound power = 150 W and pH = 8).

No.	Compound name	Structure	t _R (min)	Main fragments (m/z)/(percent)
1	Acetic acid		4.604	75.00 (100 %), 116.00 (91.09 %), 73.00 (13.02 %), 117.00 (10.24 %), 76.00 (8.56 %)
2	Benzene		5.947	105.00 (100 %), 120.00 (50.25 %), 119.00 (18.46 %), 77.00 (11.57 %), 91.00 (10.68 %)
3	Ethanamide		6.457	168.90 (100 %), 105.00 (94.22 %), 120.10 (40.33 %), 69.00 (29.35 %), 147.00 (28.44 %)
4	Ethanone		26.187	171.00 (100 %), 154.90 (53.65 %), 57.00 (13.55 %), 55.00 (12.99 %), 172.00 (9.68 %)
5	Nonanedioic acid		26.775	55.00 (100 %), 71.00 (89.14 %), 171.00 (88.46 %), 57.00 (70.70 %), 97.00 (70.41 %)
6	Cyclopropane carboxylic acid		27.219	55.00 (100 %), 57.00 (88.53 %), 171.00 (79.40 %), 69.00 (73.05 %), 71.10 (70.53 %)
7	Hexanoic acid		30.049	99.00 (100 %), 57.00 (31.05 %), 113.10 (28.20 %), 71.10 (24.82 %), 55.00 (24.72 %)
8	2-Pyranone		32.523	99.00 (100 %), 57.00 (66.67 %), 55.00 (55.15 %), 207.00 (51.69 %), 71.10 (47.90 %)
9	Methoxy acetic acid		32.701	99.00 (100 %), 57.00 (87.08 %), 207.00 (59.87%), 71.10 (58.89 %), 55.00 (55.52 %)

3.8. The antibacterial evaluations of FeCuMg and CrCuMg LDHs

As reported, the LDH structure played a crucial role in the antibacterial activity, where bacteria could be attached to the surface of LDH. Also, the surface hydroxyl groups of the LDHs can be converted into hydroxyl radicals in the solution, which can cause potential damage to the bacterial cytoplasmic membrane [59]. Moreover, transition metals such as chromium and iron intercalated to the different nanostructures can boost the antibacterial activity too [60]. In the present study, *S. aureus* as a model bacterium was used to assess the antibacterial activity of the synthesized catalysts with the catalyst dosages of 400 and 600 $\mu\text{g mL}^{-1}$. As illustrated in Fig. 12, both catalysts depicted low antibacterial activity with numerous bacterial colonies in the presence of 400 $\mu\text{g mL}^{-1}$ dosage. As shown in Fig. S4, at an optimum dosage of 600 $\mu\text{g mL}^{-1}$, the reduction in the viability of *S. aureus* were 91.3 % and 80.0 % in the presence of CrCuMg LDH and FeCuMg LDH, respectively. This result implies the higher antibacterial activity of CrCuMg LDH than that of FeCuMg LDH.

< Fig. 12 >

< Fig. S4 >

Wells including the concentrations of LDH demonstrated no turbidity after the first incubation (24 h) but showed bacterial growth on agar plate after further 24 h incubation were regarded as the minimum inhibitory concentration (MIC). Wells which didn't depict any turbidity and growth after the first and second incubations were said to have a minimum bactericidal concentration (MBC). As shown in Figs. S5a and S5b and Table 5, no turbidity was observed in the presence of 400, 200, 100, and 50 $\mu\text{g mL}^{-1}$ of FeCuMg LDH and CrCuMg LDH. Based on Fig. S5c and Table 6, 100, and 50 $\mu\text{g mL}^{-1}$ of FeCuMg LDH showed growth on an agar plate which suggested that 50 $\mu\text{g mL}^{-1}$ and 200 $\mu\text{g mL}^{-1}$ were the MIC and MBC values. From the aforementioned facts, it can be deduced that 50 $\mu\text{g mL}^{-1}$ and 100 $\mu\text{g mL}^{-1}$ were introduced as MIC and MBC in the presence of CrCuMg LDH (Fig. S5d and Table 6).

< Fig. S5>

Table 5. Inhibition pattern of *S. aureus* using different concentrations of FeCuMg and CrCuMg LDHs after 24 h incubation at 37°C.

FeCuMg LDH concentration ($\mu\text{g mL}^{-1}$)	Turbidity in broth								
	400	200	100	50	25	12.5	6.25	3.12	1.56
<i>S. aureus</i>	-	-	-	-	+	+	+	+	+
CrCuMg LDH concentration ($\mu\text{g mL}^{-1}$)	Turbidity in broth								
	400	200	100	50	25	12.5	6.25	3.12	1.56
<i>S. aureus</i>	-	-	-	-	+	+	+	+	+

+ = Growth; - = Without growth.

Table 6. The growth pattern of *S. aureus* with nutrient broth using different concentrations of FeCuMg and CrCuMg LDHs that inhibited bacteria.

FeCuMg LDH concentration ($\mu\text{g mL}^{-1}$)	Growth on agar			
	400	200	100	50
<i>S. aureus</i>	-	-	+	+
CrCuMg LDH concentration ($\mu\text{g mL}^{-1}$)	Growth on agar			
	400	200	100	50
<i>S. aureus</i>	-	-	-	+

4. Conclusions

The effectiveness of two tri-metal LDHs (FeCuMg and CrCuMg LDHs) was evaluated and compared for the sonophotocatalytic degradation of AB113 in an aquatic phase. The sonolysis (ultrasound alone) and photolysis (visible light source alone) were not effective processes for

the decolorization. The results showed more sonophotocatalytic activity of CrCuMg LDH than that of FeCuMg LDH. The results of characterization techniques including SEM, TEM, XRD, and FT-IR showed the appropriate structure of the as-synthesized layered materials; however, the results of N₂ adsorption-desorption analysis displayed the higher surface area of CrCuMg LDH in comparison with FeCuMg LDH, thereby providing more reactive sites for the formation of oxidizing radical species. For both Fe and Cr-incorporated LDHs, sonophotocatalytic activity was higher than photocatalytic and sonocatalytic activity in terms of decolorization. Reusability test results exhibited the high stability of both sonophotocatalysts within five consecutive operational runs with negligible reduction in their sonophotocatalytic activity. The addition of radical scavengers and subsequent reduction in catalytic activity demonstrated the major role of active radical species in the degradation of the target pollutant. In addition, identified intermediates generated during the sonophotocatalysis revealed favorable progress in the mineralization of the organic pollutant before being discharged into the environment. In general, Cr-incorporated LDH was more efficient than Fe-incorporated LDH for the sonocatalytic decolorization of wastewater streams. Furthermore, the examination of antibacterial activity revealed a higher ability of the CrCuMg LDH to inactivate *S. aureus* compared to FeCuMg LDH. Thus, as-synthesized layered compounds are not only able to sonophotocatalytically decolorize textile wastewaters, but also able to inactivate pathogenic microorganisms present in the wastewater before being discharged into the ecosystem. This capability improves the reusability potential of treated effluent to be used in the industrial process and other beneficial applications.

Declaration of interests

The authors declare that they have no known competing financial interests or personal relationships that could have appeared to influence the work reported in this paper.

Acknowledgments

The authors thank the support provided by the University of Tabriz, Arak University of Medical Sciences, Nanjing Forestry University [Grant Nos. 163020139 and 163020210], Science and Technology Department of Jiangsu Province (BK2020043008), National Natural Science Foundation of China (5201101466) and National Foundation of Elites.

References

- [1] L. Mohapatra, K. Parida, A review on the recent progress, challenges and perspective of layered double hydroxides as promising photocatalysts, *J. Mater. Chem. A*, 4 (2016) 10744-10766.
- [2] A. Jawad, X. Lu, Z. Chen, G. Yin, Degradation of chlorophenols by supported Co–Mg–Al layered double hydroxide with bicarbonate activated hydrogen peroxide, *J. Phys. Chem. A*, 118 (2014) 10028-10035.
- [3] M. Zubair, M. Daud, G. McKay, F. Shehzad, M.A. Al-Harhi, Recent progress in layered double hydroxides (LDH)-containing hybrids as adsorbents for water remediation, *Appl. Clay Sci.*, 143 (2017) 279-292.
- [4] L. Chagas, G. De Carvalho, W. Do Carmo, R. San Gil, S. Chiaro, A. Leitão, R. Diniz, L. De Sena, C. Achete, MgCoAl and NiCoAl LDHs synthesized by the hydrothermal urea hydrolysis method: structural characterization and thermal decomposition, *Mater. Res. Bull.*, 64 (2015) 207-215.
- [5] S. Basąg, Z. Piwowarska, A. Kowalczyk, A. Węgrzyn, R. Baran, B. Gil, M. Michalik, L. Chmielarz, Cu-Mg-Al hydroxide-like materials as precursors of effective catalysts for selective oxidation of ammonia to dinitrogen—the influence of Mg/Al ratio and calcination temperature, *Appl. Clay Sci.*, 129 (2016) 122-130.

- [6] Y.-M. Zheng, N. Li, W.-D. Zhang, Preparation of nanostructured microspheres of Zn–Mg–Al layered double hydroxides with high adsorption property, *Colloids Surf., A*, 415 (2012) 195-201.
- [7] M. Sajid, C. Basheer, Layered double hydroxides: emerging sorbent materials for analytical extractions, *Trends Anal. Chem.*, 75 (2016) 174-182.
- [8] S. Chen, F. Yang, Z. Cao, C. Yu, S. Wang, H. Zhong, Enhanced photocatalytic activity of molybdenum disulfide by compositing ZnAl–LDH, *Colloids Surf., A*, 586 (2020) 124140.
- [9] Q. Li, G. Wei, Y. Yang, Z. Li, L. Zhang, Q. Huang, Mechanochemical synthesis of Fe₂O₃/Zn–Al layered double hydroxide based on red mud, *J. Hazard. Mater.*, (2020) 122566.
- [10] G. Fan, F. Li, D.G. Evans, X. Duan, Catalytic applications of layered double hydroxides: recent advances and perspectives, *Chem. Soc. Rev.*, 43 (2014) 7040-7066.
- [11] Q. Ye, Z. Huang, P. Wu, J. Wu, J. Ma, C. Liu, S. Yang, S. Rehman, Z. Ahmed, N. Zhu, Z. Dang, Promoting the photogeneration of hydrochar reactive oxygen species based on FeAl layered double hydroxide for diethyl phthalate degradation, *J. Hazard. Mater.*, 388 (2020) 122120.
- [12] A. Halajnia, S. Oustan, N. Najafi, A. Khataee, A. Lakzian, The adsorption characteristics of nitrate on Mg–Fe and Mg–Al layered double hydroxides in a simulated soil solution, *Appl. Clay Sci.*, 70 (2012) 28-36.
- [13] H. Zeng, W. Zhang, L. Deng, J. Luo, S. Zhou, X. Liu, Y. Pei, Z. Shi, J. Crittenden, Degradation of dyes by peroxymonosulfate activated by ternary CoFeNi-layered double hydroxide: Catalytic performance, mechanism and kinetic modeling, *J. Colloid Interface Sci.*, 515 (2018) 92-100.
- [14] M. Fathinia, A. Khataee, Photocatalytic ozonation of phenazopyridine using TiO₂ nanoparticles coated on ceramic plates: mechanistic studies, degradation intermediates and ecotoxicological assessments, *Appl. Catal., A*, 491 (2015) 136-154.

- [15] R. Darvishi Cheshmeh Soltani, A.R. Khataee, H. Godini, M. Safari, M.J. Ghanadzadeh, M.S. Rajaei, Response surface methodological evaluation of the adsorption of textile dye onto biosilica/alginate nanobiocomposite: thermodynamic, kinetic, and isotherm studies, *Desalin. Water Treat.*, 56 (2015) 1389-1402.
- [16] M. Safari, A. Khataee, R. Darvishi Cheshmeh Soltani, R. Rezaee, Ultrasonically facilitated adsorption of an azo dye onto nanostructures obtained from cellulosic wastes of broom and cooler straw, *J. Colloid Interface Sci.*, 522 (2018) 228-241.
- [17] I. Michael, A. Achilleos, D. Lambropoulou, V.O. Torrens, S. Pérez, M. Petrović, D. Barceló, D. Fatta-Kassinos, Proposed transformation pathway and evolution profile of diclofenac and ibuprofen transformation products during (sono)photocatalysis, *Appl. Catal., B*, 147 (2014) 1015-1027.
- [18] X. Huang, Q. Su, S. Han, J. Zhou, G. Qian, N. Gao, Efficient activation of intercalated persulfate via a composite of reduced graphene oxide and layered double hydroxide, *J. Hazard. Mater.*, 389 (2020) 122051.
- [19] A. Zantias, Z. Frontistis, J. Vakros, O.S. Arvaniti, R.S. Ribeiro, A.M.T. Silva, J.L. Faria, H.T. Gomes, D. Mantzavinos, Degradation of methylparaben by sonocatalysis using a Co–Fe magnetic carbon xerogel, *Ultrason. Sonochem.*, 64 (2020) 105045.
- [20] K. Qi, S.-y. Liu, M. Qiu, Photocatalytic performance of TiO₂ nanocrystals with/without oxygen defects, *Chin. J. Catal.*, 39 (2018) 867-875.
- [21] S.D. Ayare, P.R. Gogate, Sonophotocatalytic oxidation based treatment of phthalocyanine pigment containing industrial wastewater intensified using oxidising agents, *Sep. Purif. Technol.*, 233 (2020) 115979.
- [22] A.V. Karim, A. Shriwastav, Degradation of ciprofloxacin using photo, sono, and sonophotocatalytic oxidation with visible light and low-frequency ultrasound: Degradation kinetics and pathways, *Chem. Eng. J.*, (2020) 124853.

- [23] Y. Ma, F. Chen, Q. Yang, Y. Zhong, X. Shu, F. Yao, T. Xie, X. Li, D. Wang, G. Zeng, Sulfate radical induced degradation of Methyl Violet azo dye with CuFe layered double hydroxide as heterogeneous photoactivator of persulfate, *J. Environ. Manage.*, 227 (2018) 406-414.
- [24] F.L. Theiss, G.A. Ayoko, R.L. Frost, Synthesis of layered double hydroxides containing Mg^{2+} , Zn^{2+} , Ca^{2+} and Al^{3+} layer cations by co-precipitation methods—A review, *Appl. Surf. Sci.*, 383 (2016) 200-213.
- [25] S. Xia, L. Zhang, X. Zhou, G. Pan, Z. Ni, The photocatalytic property for water splitting and the structural stability of CuMgM layered double hydroxides (M= Al, Cr, Fe, Ce), *Appl. Clay Sci.*, 114 (2015) 577-585.
- [26] G. Mishra, B. Dash, S. Pandey, Layered double hydroxides: A brief review from fundamentals to application as evolving biomaterials, *Appl. Clay Sci.*, 153 (2018) 172-186
- [27] D. Wang, N. Ge, S. Qian, J. Li, Y. Qiao, X. Liu, Selenium doped Ni–Ti layered double hydroxide (Ni–Ti LDH) films with selective inhibition effect to cancer cells and bacteria, *RSC Adv.*, 5 (2015) 106848-106859.
- [28] A. Khataee, S. Arefi-Oskoui, L. Samaei, ZnFe–Cl nanolayered double hydroxide as a novel catalyst for sonocatalytic degradation of an organic dye, *Ultrason. Sonochem.*, 40 (2018) 703-713.
- [29] R. Abazari, A.R. Mahjoub, S. Sanati, Z. Rezvani, Z. Hou, H. Dai, Ni–Ti layered double hydroxide@graphitic carbon nitride nanosheet: A novel nanocomposite with high and ultrafast sonophotocatalytic performance for degradation of antibiotics, *Inorg. Chem.*, 58 (2019) 1834-1849.
- [30] K. Harada, T.K.N. Nguyen, Y. Matsui, K. Fujii, F. Grasset, N. Ohashi, M. Matsuda, T. Uchikoshi, Observation of stacking faults and photoluminescence of laurate ion intercalated Zn/Al layered double hydroxide, *Mater. Lett.*, 213 (2018) 323-325.

- [31] M. Shao, J. Han, M. Wei, D.G. Evans, X. Duan, The synthesis of hierarchical Zn–Ti layered double hydroxide for efficient visible-light photocatalysis, *Chem. Eng. J.*, 168 (2011) 519-524.
- [32] P.Y. Motlagh, A. Khataee, A. Hassani, T. Sadeghi Rad, ZnFe-LDH/GO nanocomposite coated on the glass support as a highly efficient catalyst for visible light photodegradation of an emerging pollutant, *J. Mol. Liq.*, 302 (2020) 112532.
- [33] A. Hassani, M. Kiranşan, R. Darvishi Cheshmeh Soltani, A. Khataee, S. Karaca, Optimization of the adsorption of a textile dye onto nanoclay using a central composite design, *Turk. J. Chem.*, 39 (2015) 734-749.
- [34] Y. Chen, J. Yan, D. Ouyang, L. Qian, L. Han, M. Chen, Heterogeneously catalyzed persulfate by CuMgFe layered double oxide for the degradation of phenol, *Appl. Catal., A*, 538 (2017) 19-26.
- [35] S. Said, M. Elhossieny, M. Riad, S. Mikhail, Pristine Cu (Co)/Fe layered double hydroxides (Co (Cu)/Fe-LDH) as active catalysts for the transalkylation of toluene to trimethylbenzenes, *Mol. Catal.*, 445 (2018) 213-222.
- [36] P. Gholami, L. Dinpazhoh, A. Khataee, A. Hassani, A. Bhatnagar, Facile hydrothermal synthesis of novel Fe-Cu layered double hydroxide/biochar nanocomposite with enhanced sonocatalytic activity for degradation of cefazolin sodium, *J. Hazard. Mater.*, (2019) 120742.
- [37] Y. Liu, Y. Guo, Y. Liu, X. Xu, H. Peng, X. Fang, X. Wang, SnO₂ nano-rods promoted by In, Cr and Al cations for toluene total oxidation: The impact of oxygen property and surface acidity on the catalytic activity, *Appl. Surf. Sci.*, 420 (2017) 186-195.
- [38] T.S. Rad, A. Khataee, S.R. Pouran, Synergistic enhancement in photocatalytic performance of Ce (IV) and Cr (III) co-substituted magnetite nanoparticles loaded on reduced graphene oxide sheets, *J. Colloid Interface Sci.*, 528 (2018) 248-262.

- [39] H. Huang, R. Cao, S. Yu, K. Xu, W. Hao, Y. Wang, F. Dong, T. Zhang, Y. Zhang, Single-unit-cell layer established Bi_2WO_6 3D hierarchical architectures: Efficient adsorption, photocatalysis and dye-sensitized photoelectrochemical performance, *Appl. Catal., B*, 219 (2017) 526-537.
- [40] J. Monteagudo, H. El-Taliawy, A. Durán, G. Caro, K. Bester, Sono-activated persulfate oxidation of diclofenac: Degradation, kinetics, pathway and contribution of the different radicals involved, *J. Hazard. Mater.*, 357 (2018) 457-465.
- [41] R. Hassandoost, S.R. Pourn, A. Khataee, Y. Orooji, S.W. Joo, Hierarchically structured ternary heterojunctions based on $\text{Ce}^{3+}/\text{Ce}^{4+}$ modified Fe_3O_4 nanoparticles anchored onto graphene oxide sheets as magnetic visible-light-active photocatalysts for decontamination of oxytetracycline, *J. Hazard. Mater.*, 376 (2019) 200-211.
- [42] M.M. Mohamed, M.A. Ghanem, M. Khairy, E. Naguib, N.H. Alotaibi, Zinc oxide incorporated carbon nanotubes or graphene oxide nanohybrids for enhanced sonophotocatalytic degradation of methylene blue dye, *Appl. Surf. Sci.*, 487 (2019) 539-549.
- [43] D. Panda, S. Manickam, Recent advancements in the sonophotocatalysis (SPC) and doped-sonophotocatalysis (DSPC) for the treatment of recalcitrant hazardous organic water pollutants, *Ultrason. Sonochem.*, 36 (2017) 481-496.
- [44] H. Daneshvar, M.S. Dorraji, A. Amani-Ghadim, M. Rasoulifard, Enhanced sonocatalytic performance of ZnTi nano-layered double hydroxide by substitution of Cu (II) cations, *Ultrason. Sonochem.*, 58 (2019) 104632.
- [45] A. Mehrizad, M.A. Behnajady, P. Gharbani, S. Sabbagh, Sonocatalytic degradation of Acid Red 1 by sonochemically synthesized zinc sulfide-titanium dioxide nanotubes: Optimization, kinetics and thermodynamics studies, *J. Cleaner Prod.*, 215 (2019) 1341-1350.

- [46] P. Yekan Motlagh, A. Khataee, T. Sadeghi Rad, A. Hassani, S.W. Joo, Fabrication of ZnFe-layered double hydroxides with graphene oxide for efficient visible light photocatalytic performance, *J. Taiwan Inst. Chem. Eng.*, 101 (2019) 186-203.
- [47] J. Yan, Y. Chen, L. Qian, W. Gao, D. Ouyang, M. Chen, Heterogeneously catalyzed persulfate with a CuMgFe layered double hydroxide for the degradation of ethylbenzene, *J. Hazard. Mater.*, 338 (2017) 372-380.
- [48] X. Wang, P. Wu, Y. Lu, Z. Huang, N. Zhu, C. Lin, Z. Dang, NiZnAl layered double hydroxides as photocatalyst under solar radiation for photocatalytic degradation of orange G, *Sep. Purif. Technol.*, 132 (2014) 195-205.
- [49] G. Chen, S. Qian, X. Tu, X. Wei, J. Zou, L. Leng, S. Luo, Enhancement photocatalytic degradation of rhodamine B on nanoPt intercalated Zn-Ti layered double hydroxides, *Appl. Surf. Sci.*, 293 (2014) 345-351.
- [50] A. Khataee, T. Sadeghi Rad, S. Nikzat, A. Hassani, M.H. Aslan, M. Kobya, E. Demirbaş, Fabrication of NiFe layered double hydroxide/reduced graphene oxide (NiFe-LDH/rGO) nanocomposite with enhanced sonophotocatalytic activity for the degradation of moxifloxacin, *Chem. Eng. J.*, 375 (2019) 122102.
- [51] A. Hassani, P. Eghbali, Ö. Metin, Sonocatalytic removal of methylene blue from water solution by cobalt ferrite/mesoporous graphitic carbon nitride (CoFe₂O₄/mpg-C₃N₄) nanocomposites: response surface methodology approach, *Environ. Sci. Pollut. Res.*, 25 (2018) 32140-32155.
- [52] C. Gong, F. Chen, Q. Yang, K. Luo, F. Yao, S. Wang, X. Wang, J. Wu, X. Li, D. Wang, Heterogeneous activation of peroxymonosulfate by Fe-Co layered double hydroxide for efficient catalytic degradation of Rhoadmine B, *Chem. Eng. J.*, 321 (2017) 222-232.

- [53] N. Li, Z. Chang, H. Dang, Y. Zhan, J. Lou, S. Wang, S. Attique, W. Li, H. Zhou, C. Sun, Deep eutectic solvents assisted synthesis of MgAl layered double hydroxide with enhanced adsorption toward anionic dyes, *Colloids Surf., A*, 591 (2020) 124507.
- [54] P. Wang, D.H.L. Ng, M. Zhou, J. Li, Freely standing MgAl-layered double hydroxides nanosheets and their derived metal oxides on g-C₃N₄ thin-layer designed for obtaining synergic effect of adsorption and photocatalysis, *Appl. Clay Sci.*, 178 (2019) 105131.
- [55] A. Samad, S. Ahsan, I. Tateishi, M. Furukawa, H. Katsumata, T. Suzuki, S. Kaneco, Indirect photocatalytic reduction of arsenate to arsenite in aqueous solution with TiO₂ in the presence of hole scavengers, *Chin. J. Chem. Eng.*, 26 (2018) 529-533.
- [56] C. Zhang, Y. Dong, B. Li, F. Li, Comparative study of three solid oxidants as substitutes of H₂O₂ used in Fe (III)-oxalate complex mediated Fenton system for photocatalytic elimination of reactive azo dye, *J. Cleaner Prod.*, 177 (2018) 245-253.
- [57] G. Eshaq, A.E. ElMetwally, (Mg–Zn)–Al layered double hydroxide as a regenerable catalyst for the catalytic glycolysis of polyethylene terephthalate, *J. Mol. Liq.*, 214 (2016) 1-6.
- [58] L. Tian, Y. Zhao, S. He, M. Wei, X. Duan, Immobilized Cu–Cr layered double hydroxide films with visible-light responsive photocatalysis for organic pollutants, *Chem. Eng. J.*, 184 (2012) 261-267.
- [59] S.A. Moaty, A. Farghali, R. Khaled, Preparation, characterization and antimicrobial applications of Zn-Fe LDH against MRSA, *Mater. Sci. Eng. C*, 68 (2016) 184-193.
- [60] M.A. Ansari, A. Baykal, S. Asiri, S. Rehman, Synthesis and characterization of antibacterial activity of spinel chromium-substituted copper ferrite nanoparticles for biomedical application, *J. Inorg. Organomet. Polym Mater.*, 28 (2018) 2316-2327.

Fig. 1. SEM images of FeCuMg LDH (a and b) and CrCuMg LDH (c and d).

Fig. 2. HRTEM images of FeCuMg LDH (a) and CrCuMg LDH (b).

Fig. 3. EDX of FeCuMg (a) and CrCuMg LDHs (b), XRD patterns of LDHs (c), FT-IR of LDHs (d), along with XPS spectra of FeCuMg LDH (e) and CrCuMg LDH (f).

Fig. 4. Degradation potential of AB113 by various processes (operational parameters: (a) [FeCuMg] = 0.5 g L⁻¹, ultrasonic power = 150 W, [AB113] = 50 mg L⁻¹ and pH = 8; and (b) [CrCuMg] = 0.5 g L⁻¹, ultrasonic power = 150 W, [AB113] = 50 mg L⁻¹ and pH = 8), along with $(\alpha h\nu)^2 - h\nu$ curves of FeCuMg (c) and CrCuMg LDHs (d).

Fig. 5. Effect of the pollutant concentration (operational parameters: (a) [FeCuMg] = 0.5 g L⁻¹, ultrasonic power = 150 W, [AB113] = 40, 50, 60 and 70 mg L⁻¹ and pH = 8; and (b) [CrCuMg] = 0.5 g L⁻¹, ultrasonic power = 150 W, [AB113] = 40, 50, 60 and 70 mg L⁻¹ and pH = 8).

Fig. 6. Effect of the catalyst concentration (operational parameters: (a) [FeCuMg] = 0.1, 0.3, 0.5, 0.7 and 1 g L⁻¹, ultrasonic power = 150 W, [AB113] = 50 mg L⁻¹ and pH = 8; and (b) [CrCuMg] = 0.1, 0.3, 0.5, 0.7 and 1 g L⁻¹, ultrasonic power = 150 W, [AB113] = 50 mg L⁻¹ and pH = 8).

Fig. 7. Effect of pH (operational parameters: (a) [FeCuMg] = 0.5 g L⁻¹, ultrasonic power = 150 W, [AB113] = 50 mg L⁻¹ and pH = 4, 6, 8 and 13; (b) pH_{pzc} of FeCuMg LDH; (c) [CrCuMg] = 0.5 g L⁻¹, ultrasonic power = 150 W, [AB113] = 50 mg L⁻¹ and pH = 4, 6, 8 and 13; and (d) pH_{pzc} of CrCuMg LDH).

Fig. 8. Effect of ultrasonic power (operational parameters: (a) [FeCuMg] = 0.5 g L⁻¹, ultrasonic power = 150, 200 and 300 W, [AB113] = 50 mg L⁻¹ and pH = 8; and (b) [CrCuMg] = 0.5 g L⁻¹, ultrasonic power = 150, 200 and 300 W, [AB113] = 50 mg L⁻¹ and pH = 8).

Fig. 9. Effect of the presence of various scavengers on the degradation efficiency of AB113 by both FeCuMg LDH [(a-1) and (b-1)] and CrCuMg LDH [(a-2) and (b-2)] under different molar

ratios of 1:1 and 1:10. Operational parameters: [sonophotocatalyst] = 0.5 g L⁻¹, ultrasonic power = 150 W, [AB113] = 50 mg L⁻¹ and pH = 8.

Fig. 10. Effect of various enhancers on the sonophotocatalytic degradation efficiency of AB113 over FeCuMg LDH (a) and CrCuMg LDH (b). Operational parameters: [sonophotocatalyst] = 0.5 g L⁻¹, ultrasonic power = 150 W, [AB113] = 50 mg L⁻¹ and pH = 8.

Fig. 11. Reusability test results for FeCuMg LDH (a) and CrCuMg LDH (b). Operational parameters: [sonophotocatalyst] = 0.5 g L⁻¹, ultrasonic power = 150 W, [AB113] = 50 mg L⁻¹ and pH = 8.

Fig. 12. Images demonstrating the influence of FeCuMg LDH and CrCuMg LDH (400 and 600 µg mL⁻¹) on the number of CFU.

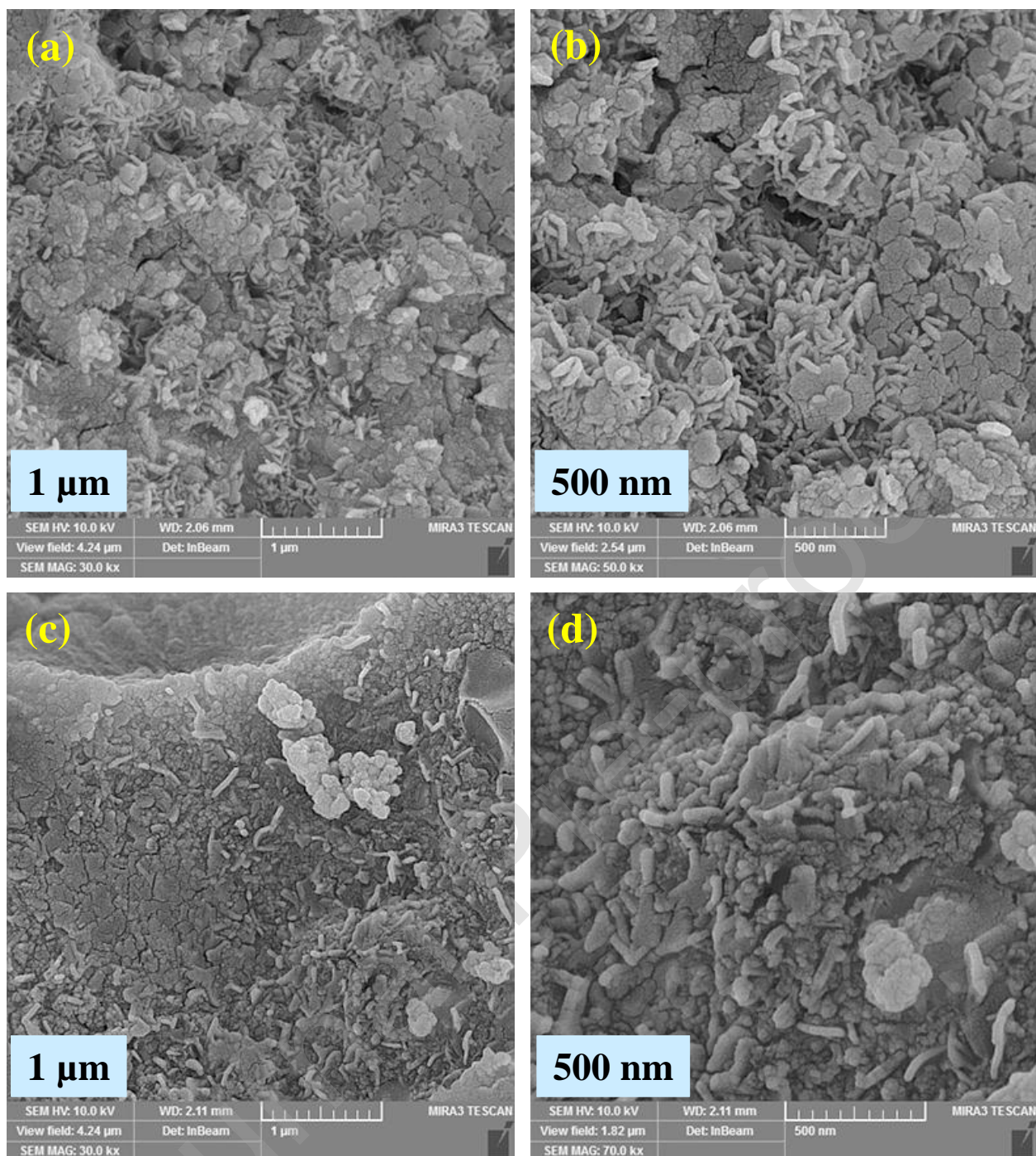


Fig. 1. SEM images of FeCuMg LDH (a and b) and CrCuMg LDH (c and d).

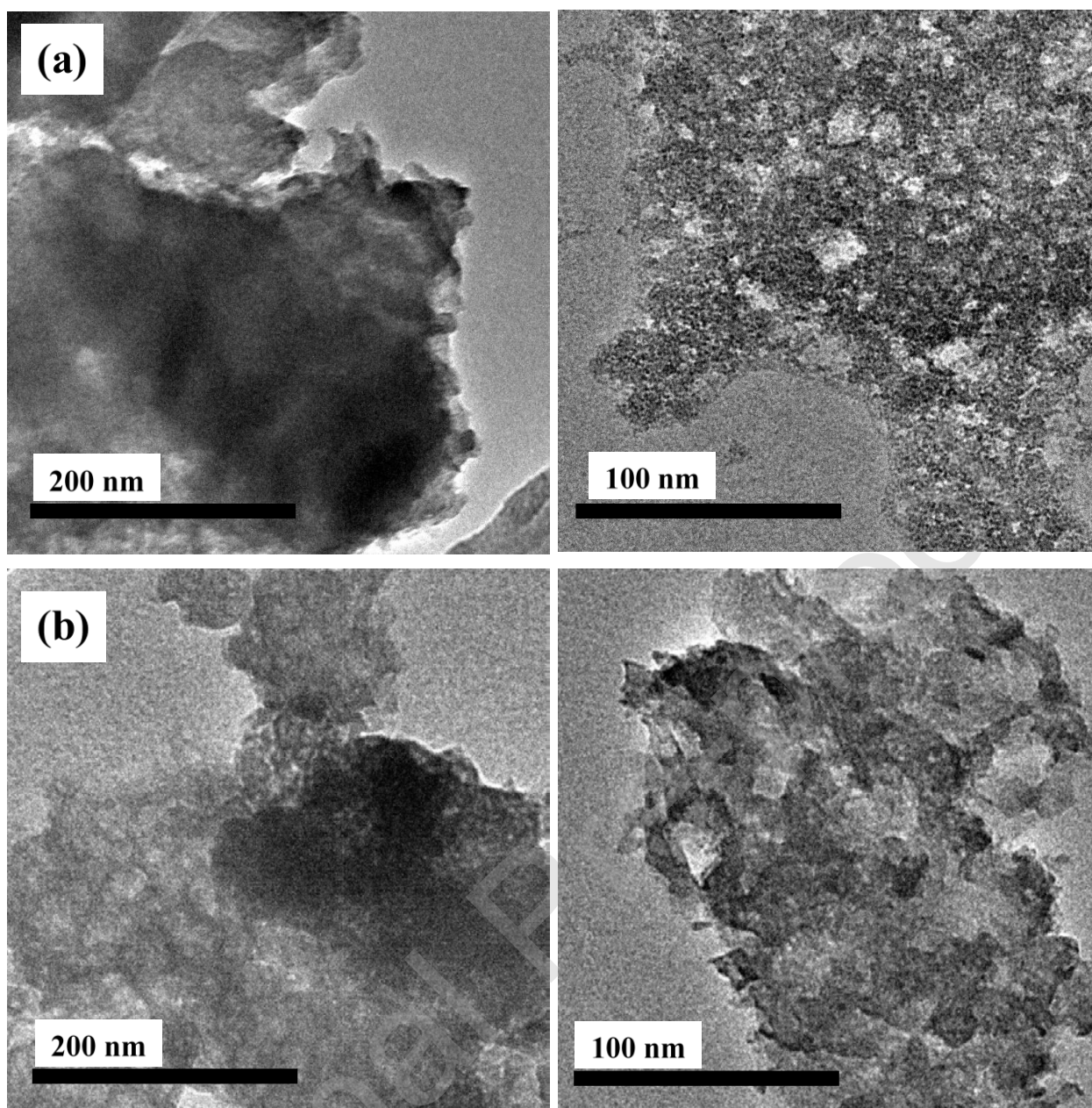


Fig. 2. HRTEM images of FeCuMg LDH (a) and CrCuMg LDH (b).

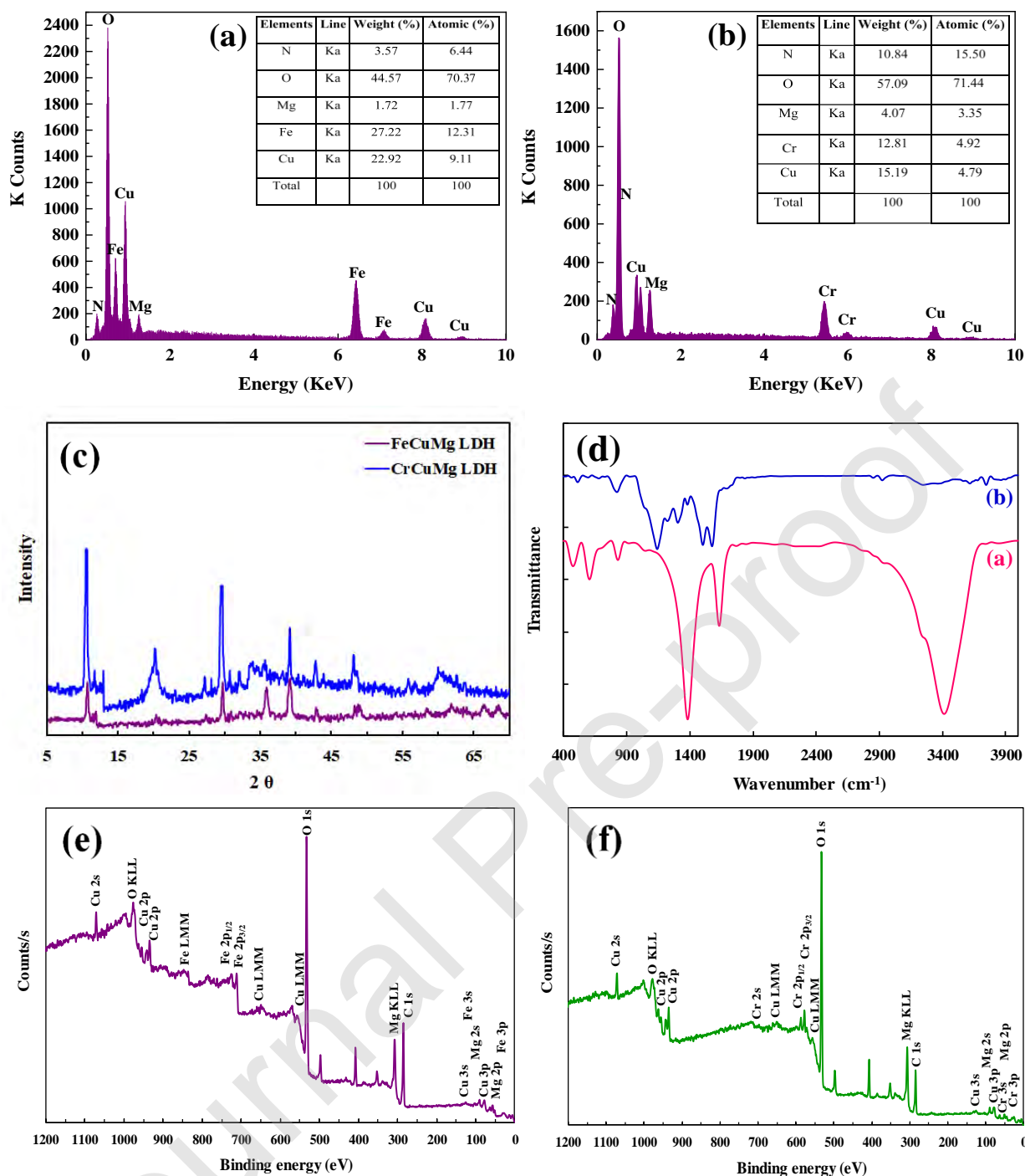


Fig. 3. EDX of FeCuMg (a) and CrCuMg LDHs (b), XRD patterns of LDHs (c), FT-IR of LDHs (d), along with XPS spectra of FeCuMg LDH (e) and CrCuMg LDH (f).

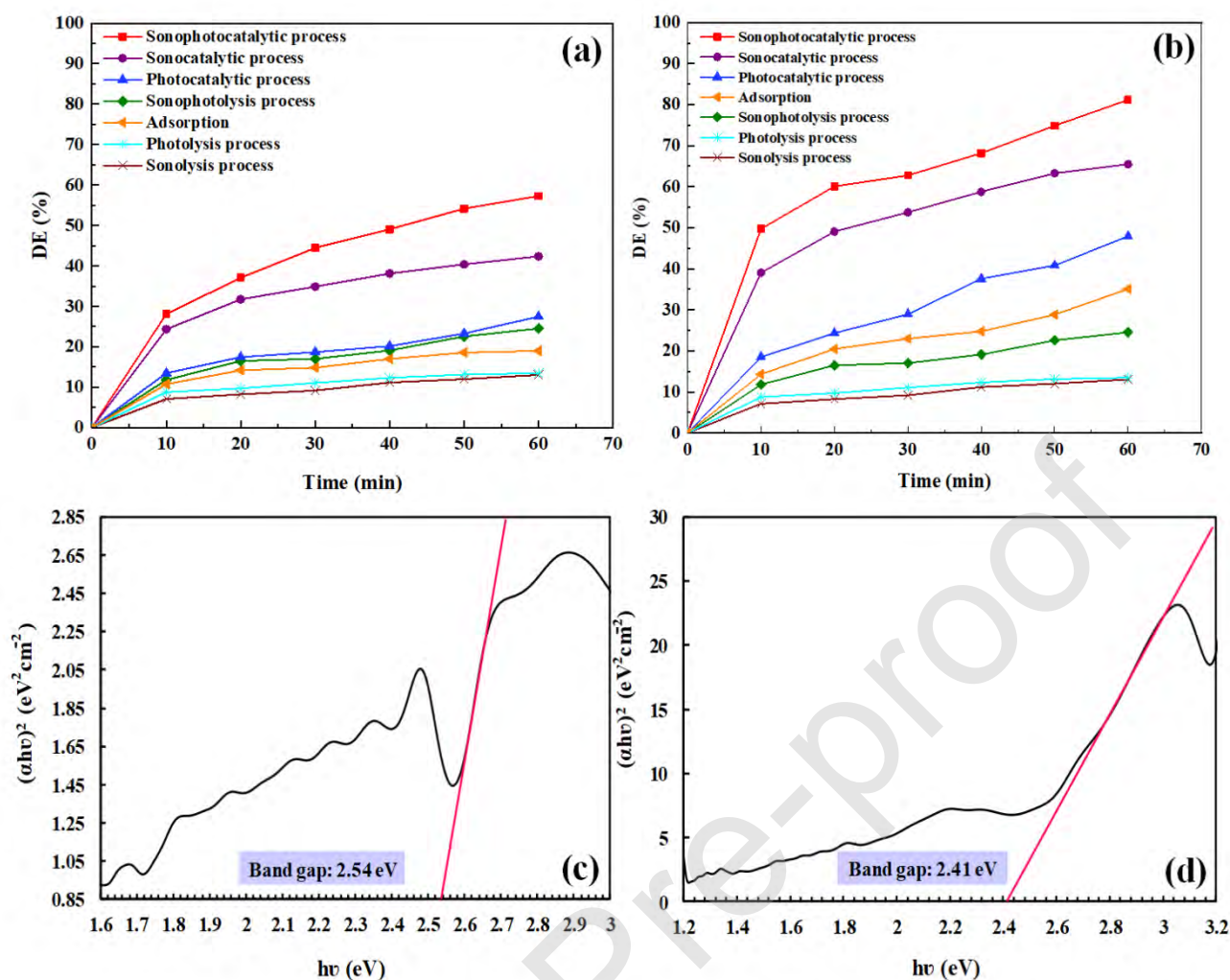


Fig. 4. Degradation potential of AB113 by various processes (operational parameters: (a) $[\text{FeCuMg}] = 0.5 \text{ g L}^{-1}$, ultrasonic power = 150 W, $[\text{AB113}] = 50 \text{ mg L}^{-1}$ and $\text{pH} = 8$; and (b) $[\text{CrCuMg}] = 0.5 \text{ g L}^{-1}$, ultrasonic power = 150 W, $[\text{AB113}] = 50 \text{ mg L}^{-1}$ and $\text{pH} = 8$), along with $(\alpha h\nu)^2$ - $h\nu$ curves of FeCuMg (c) and CrCuMg LDHs (d).

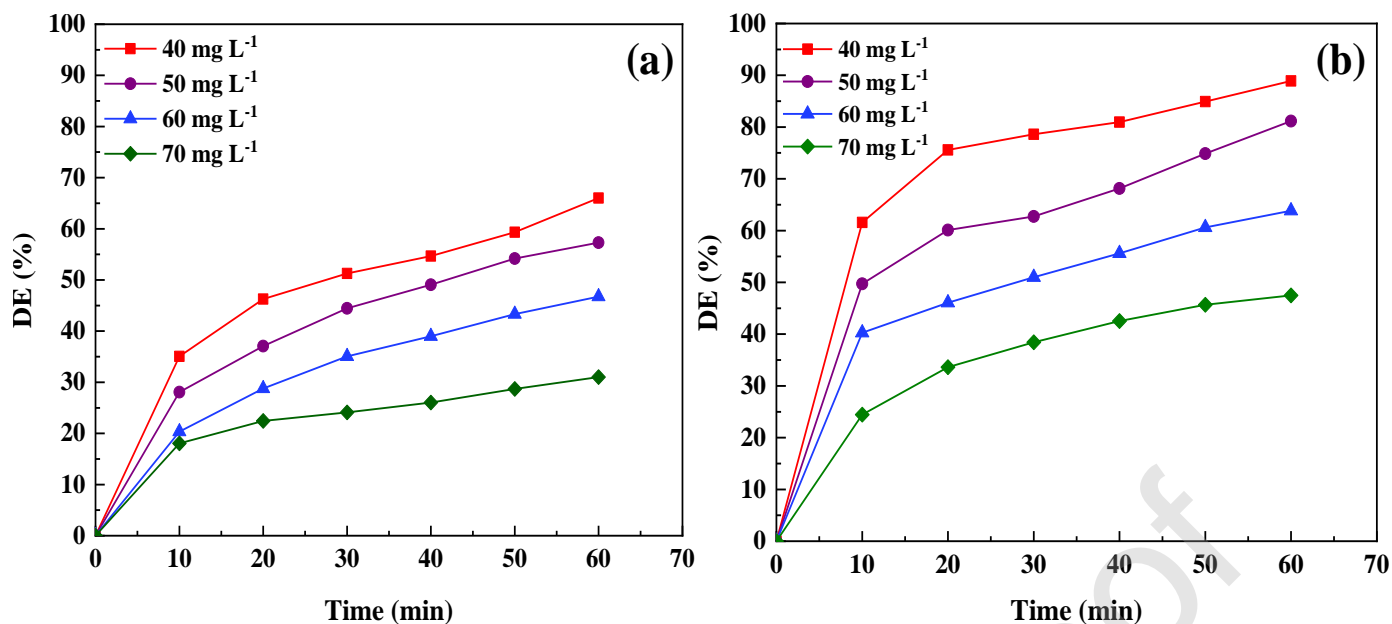


Fig. 5. Effect of the pollutant concentration (operational parameters: (a) [FeCuMg] = 0.5 g L⁻¹, ultrasonic power = 150 W, [AB113] = 40, 50, 60 and 70 mg L⁻¹ and pH = 8; and (b) [CrCuMg] = 0.5 g L⁻¹, ultrasonic power = 150 W, [AB113] = 40, 50, 60 and 70 mg L⁻¹ and pH = 8).

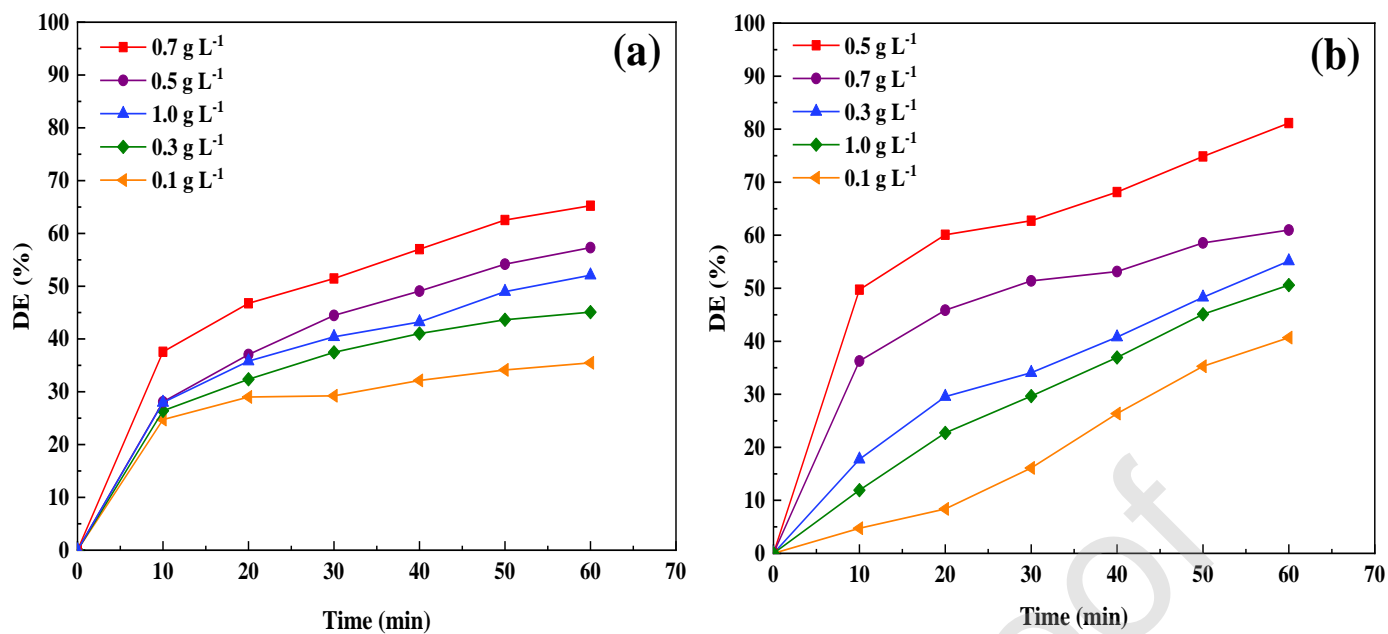


Fig. 6. Effect of the catalyst concentration (operational parameters: (a) $[\text{FeCuMg}] = 0.1, 0.3, 0.5, 0.7$ and 1 g L^{-1} , ultrasonic power = 150 W , $[\text{AB113}] = 50 \text{ mg L}^{-1}$ and $\text{pH} = 8$; and (b) $[\text{CrCuMg}] = 0.1, 0.3, 0.5, 0.7$ and 1 g L^{-1} , ultrasonic power = 150 W , $[\text{AB113}] = 50 \text{ mg L}^{-1}$ and $\text{pH} = 8$).

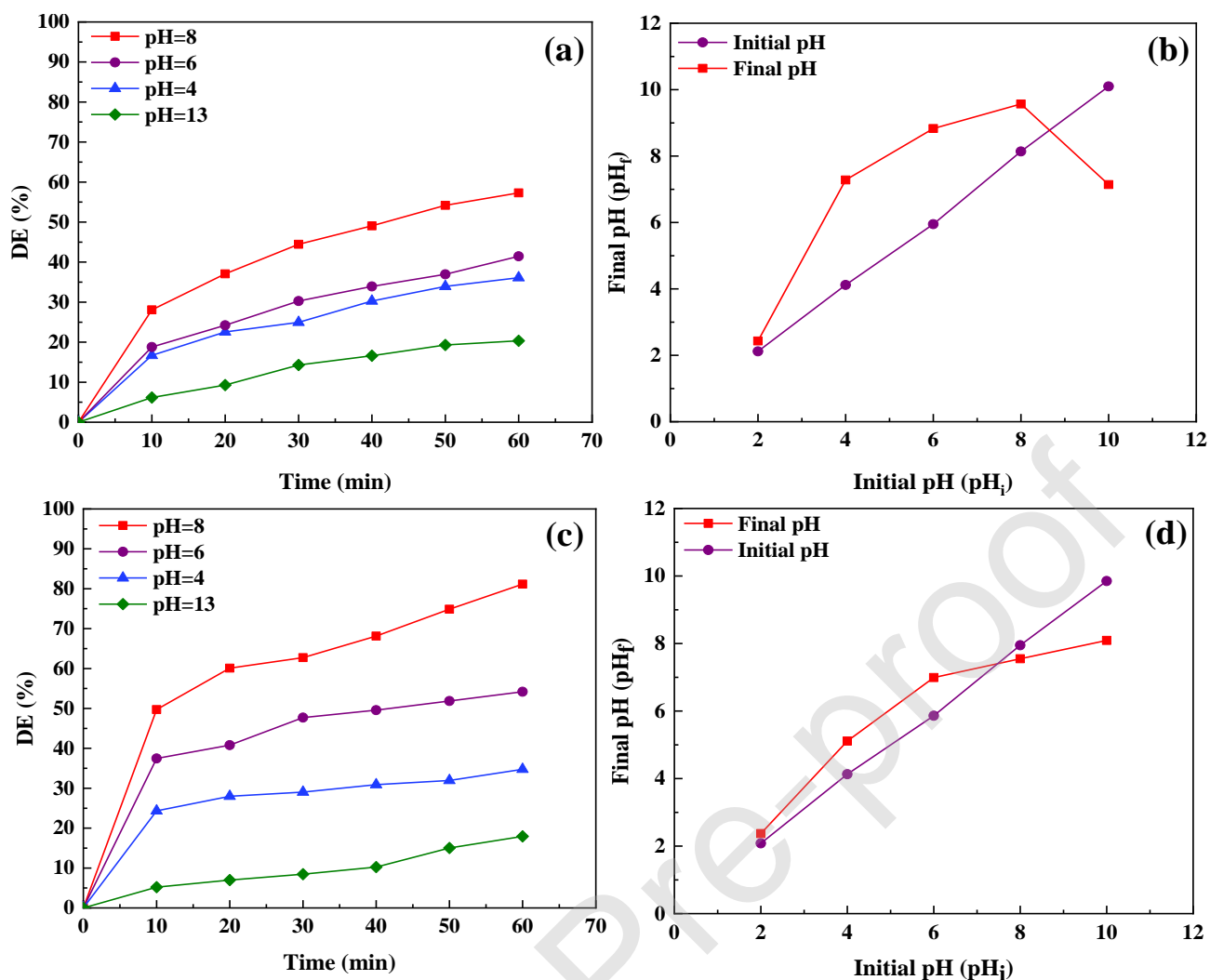


Fig. 7. Effect of pH (operational parameters: (a) $[\text{FeCuMg}] = 0.5 \text{ g L}^{-1}$, ultrasonic power = 150 W, $[\text{AB113}] = 50 \text{ mg L}^{-1}$ and pH = 4, 6, 8 and 13; (b) pH_{pzc} of FeCuMg LDH; (c) $[\text{CrCuMg}] = 0.5 \text{ g L}^{-1}$, ultrasonic power = 150 W, $[\text{AB113}] = 50 \text{ mg L}^{-1}$ and pH = 4, 6, 8 and 13; and (d) pH_{pzc} of CrCuMg LDH).

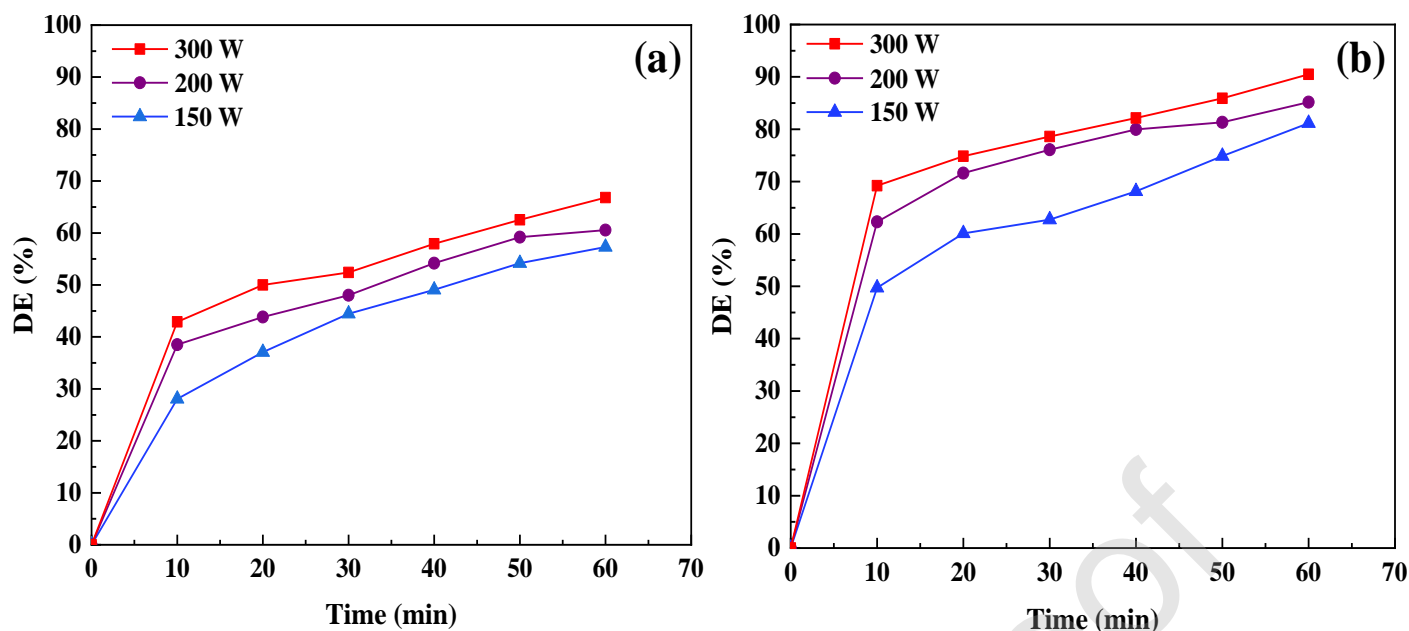


Fig. 8. Effect of ultrasonic power (operational parameters: (a) $[\text{FeCuMg}] = 0.5 \text{ g L}^{-1}$, ultrasonic power = 150, 200 and 300 W, $[\text{AB113}] = 50 \text{ mg L}^{-1}$ and $\text{pH} = 8$; and (b) $[\text{CrCuMg}] = 0.5 \text{ g L}^{-1}$, ultrasonic power = 150, 200 and 300 W, $[\text{AB113}] = 50 \text{ mg L}^{-1}$ and $\text{pH} = 8$).

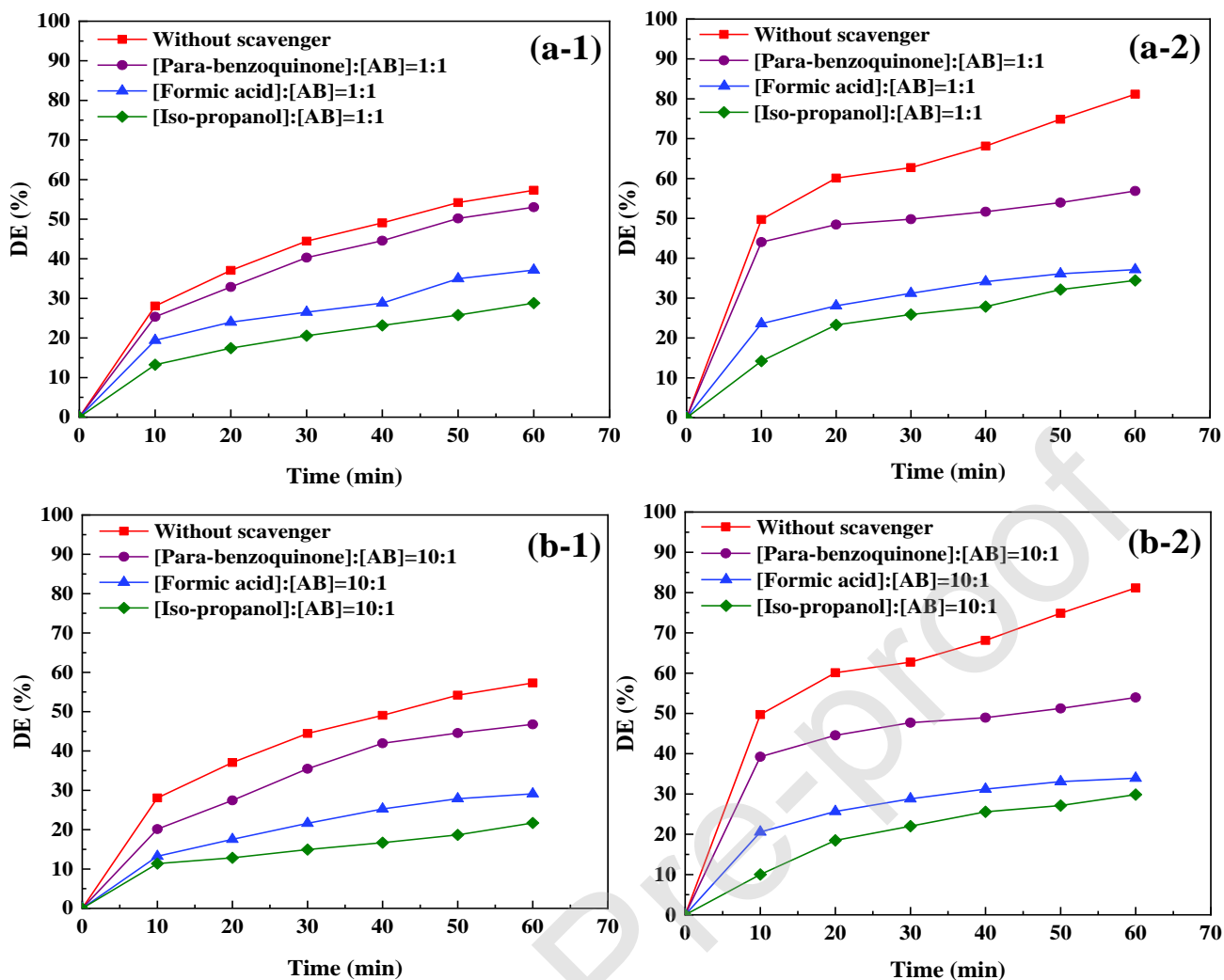


Fig. 9. Effect of the presence of various scavengers on the degradation efficiency of AB113 by both FeCuMg LDH [(a-1) and (b-1)] and CrCuMg LDH [(a-2) and (b-2)] under different molar ratios of 1:1 and 1:10 (Operational parameters: [sonophotocatalyst] = 0.5 g L⁻¹, ultrasonic power = 150 W, [AB113] = 50 mg L⁻¹ and pH = 8).

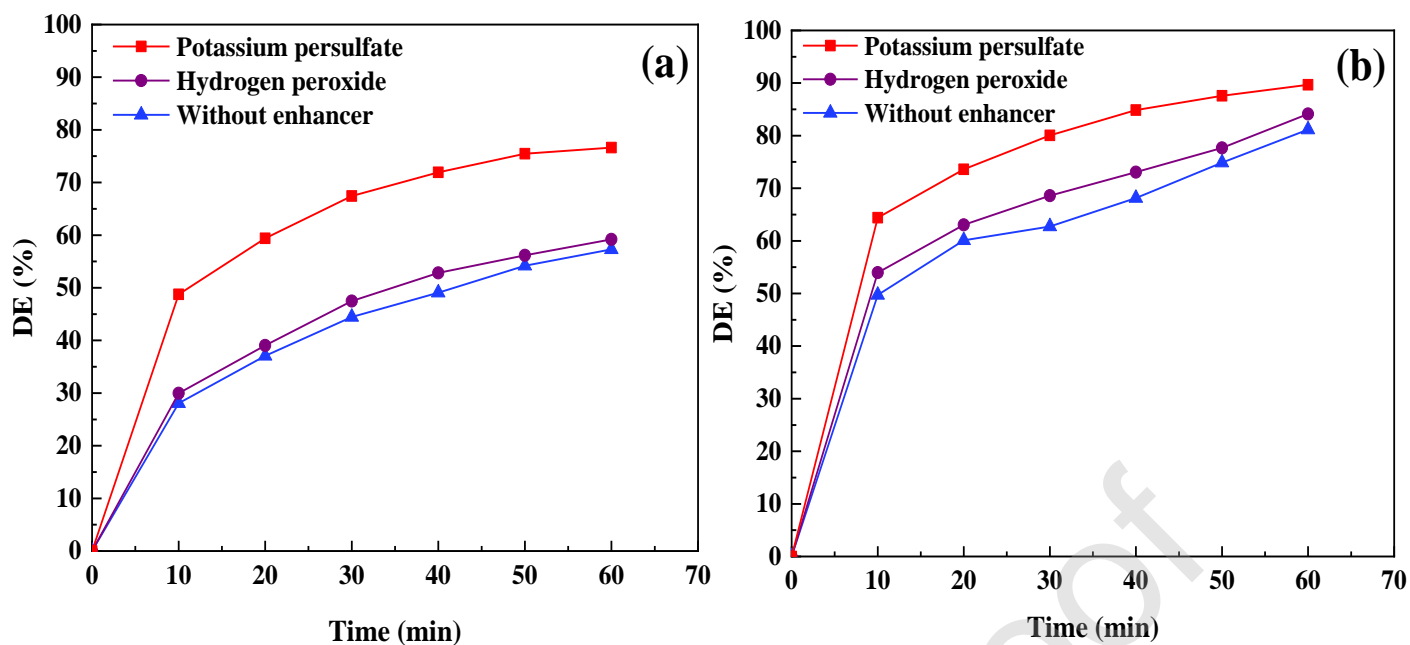


Fig. 10. Effect of various enhancers on the sonophotocatalytic degradation efficiency of AB113 over FeCuMg LDH (a) and CrCuMg LDH (b) (Operational parameters: [sonophotocatalyst] = 0.5 g L^{-1} , ultrasonic power = 150 W, [AB113] = 50 mg L^{-1} and pH = 8).

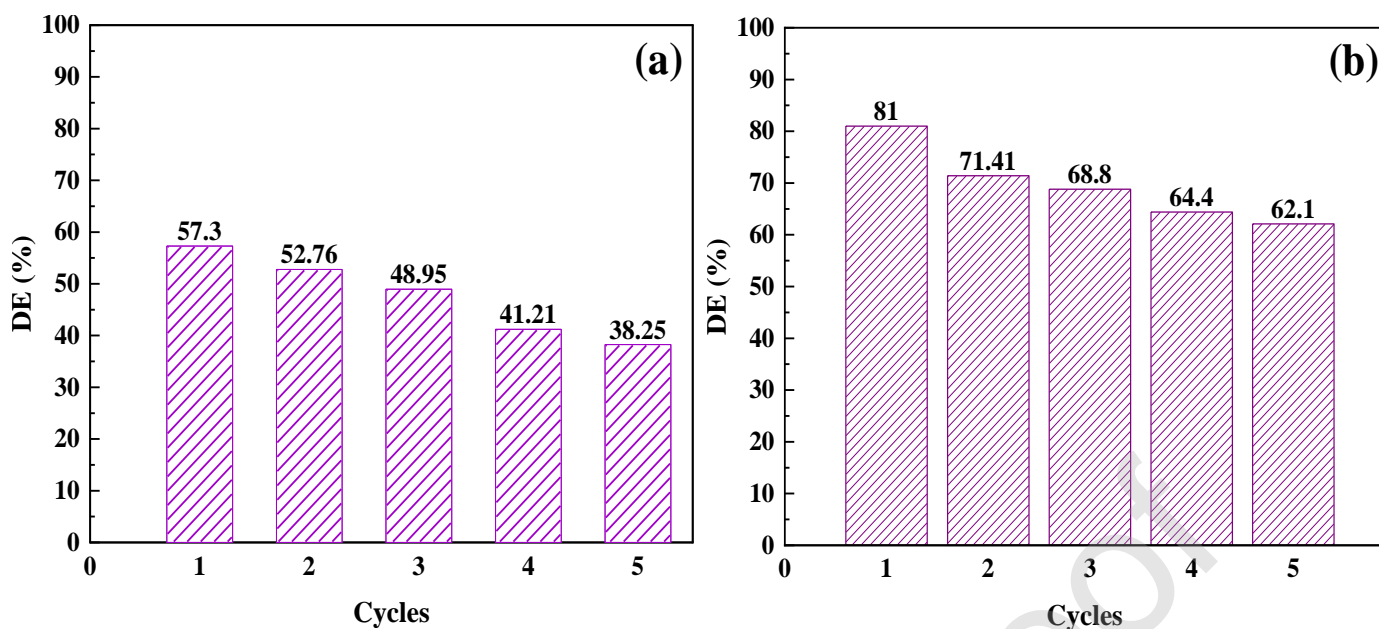


Fig. 11. Reusability test results for FeCuMg LDH (a) and CrCuMg LDH (b) (Operational parameters: [sonophotocatalyst] = 0.5 g L⁻¹, ultrasonic power = 150 W, [AB113] = 50 mg L⁻¹ and pH = 8).

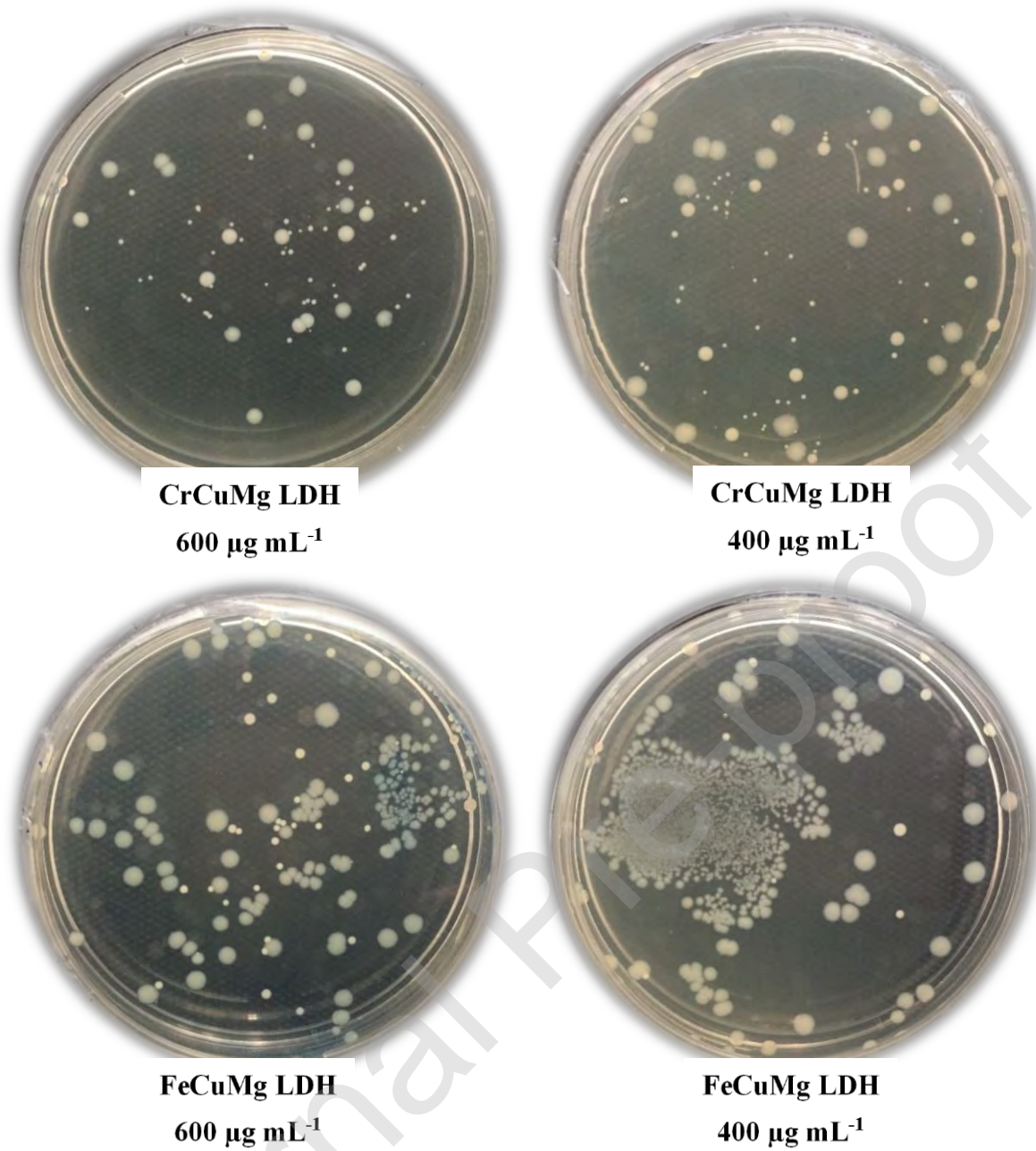


Fig. 12. Images demonstrating the influence of FeCuMg LDH and CrCuMg LDH (400 and 600 $\mu\text{g mL}^{-1}$) on the number of CFU.